ARL-TR-9116 ● Nov 2020

DEVCOM ARMY RESEARCH LABORATORY

Development and Assessment of Uniaxial Densification Limit Models for Particulate Bodies with Mono- and Bimodal-Sized Rigid Spherical Inclusions

by Jerry C LaSalvia, Anthony A DiGiovanni, and Matthew C Guziewski

NOTICES
Disclaimers

The findings in this report are not to be construed as an official Department of the Army position unless so designated by other authorized documents.

Citation of manufacturer's or trade names does not constitute an official endorsement or approval of the use thereof.

Destroy this report when it is no longer needed. Do not return it to the originator.

ARL-TR-9116 ● Nov 2020

Development and Assessment of Uniaxial Densification Limit Models for Particulate Bodies with Mono- and Bimodal-Sized Rigid Spherical Inclusions

Jerry C LaSalvia, Anthony A DiGiovanni, and Matthew C Guziewski
Weapons and Material Research Directorate, DEVCOM Army Research Laboratory

REPORT DOCUMENTATION PAGE		Form Approved OMB No. 0704-0188

1. REPORT DATE *(DD-MM-YYYY)*	2. REPORT TYPE	3. DATES COVERED (From - To)
November 2020	Technical Report	1 October 2018–30 September 2020

4. TITLE AND SUBTITLE
Development and Assessment of Uniaxial Densification Limit Models for Particulate Bodies with Mono- and Bimodal-Sized Rigid Spherical Inclusions

5a. CONTRACT NUMBER

5b. GRANT NUMBER

5c. PROGRAM ELEMENT NUMBER

6. AUTHOR(S)
Jerry C LaSalvia, Anthony A DiGiovanni, and Matthew C Guziewski

5d. PROJECT NUMBER

5e. TASK NUMBER

5f. WORK UNIT NUMBER

7. PERFORMING ORGANIZATION NAME(S) AND ADDRESS(ES)
CCDC Army Research Laboratory
ATTN: FCDD-RLW-ME
Aberdeen Proving Ground, MD 21005

8. PERFORMING ORGANIZATION REPORT NUMBER
ARL-TR-9116

9. SPONSORING/MONITORING AGENCY NAME(S) AND ADDRESS(ES)

10. SPONSOR/MONITOR'S ACRONYM(S)

11. SPONSOR/MONITOR'S REPORT NUMBER(S)

12. DISTRIBUTION/AVAILABILITY STATEMENT
Approved for public release; distribution is unlimited.

13. SUPPLEMENTARY NOTES
ORCID IDs: Anthony A DiGiovanni, 0000-0003-3344-1753; Matthew C Guziewski, 0000-0002-5761-720X

14. ABSTRACT
Ceramics reinforced with diamond inclusions are attractive armor materials due to significant enhancements in hardness. Because hardness depends on the inclusion content, the question that naturally arises is what is the inclusion content limit for a composite particulate body undergoing densification? The answer to which lies within percolation theory. During densification, if the inclusion content exceeds a critical value, a rigid percolated inclusion network forms spanning the shrinking dimension(s) of the densifying body resulting in an abrupt end to densification. This critical value is called the percolation threshold. Formulating the problem in terms of averaged characteristic quantities and making key assumptions, the mathematical challenges of percolation theory are avoided, enabling the development of deterministic models for the uniaxial densification of composite particulate bodies with either mono-sized or bimodal-sized rigid inclusions. Using the models as guidance, hot-pressing experiments were conducted on silicon hexaboride/diamond inclusion powder mixtures to validate model predictions. Overall, model predictions were in excellent agreement with the experimental results. The highest contents achieved were approximately 30 and 40 vol% for mono-sized and bimodal-sized diamond inclusions, respectively. Discrepancies between model and experimental results for bimodal-sized diamond indicate the effects of finite particle size differences cannot be disregarded as was assumed.

15. SUBJECT TERMS
diamond-inclusion-reinforced ceramics, theoretical limit for diamond content, mono-sized, bimodal-sized, densification, percolation threshold, deterministic models, experimental validation

16. SECURITY CLASSIFICATION OF:			17. LIMITATION OF ABSTRACT	18. NUMBER OF PAGES	19a. NAME OF RESPONSIBLE PERSON
a. REPORT	b. ABSTRACT	c. THIS PAGE			Jerry C LaSalvia
Unclassified	Unclassified	Unclassified	UU	55	19b. TELEPHONE NUMBER (Include area code) (410) 306-0745

Contents

List of Figures

1. Introduction and Background

It can generally be agreed upon that both low density and high hardness* are two of the most important properties that a ceramic must possess for developing high mass efficiency personnel protection technologies regardless of the kinetic energy threat, performance requirements, and system configuration.[1–11] Low density implies lighter component weight based on thickness, while a high hardness implies greater penetration resistance and disruptive capability such as fracturing of the projectile core.[7,11] High resistances to fracture, fragmentation, and granular flow are also highly desirable[12–18]; however, these are achieved through microstructural engineering that can have offsetting effects on both density and hardness.[17,19–22] As a result, their importance has been less well known and understood.

The most-common low-density ceramics used for armor applications include aluminum oxide (Al_2O_3), boron carbide (B_4C), and silicon carbide (SiC).[4–11,16–22] Depending upon load, the Vickers and Knoop hardnesses of B_4C and SiC are generally in the range of 20–30 GPa,[22–24] while Al_2O_3 ranges from 15–20 GPa depending upon glassy silicate content.[25,26] With respect to the measured hardness values of other bulk materials, only diamond and cubic boron nitride (CBN) possess higher hardness values (~100 and 60–80 GPa, respectively[27,28]). Because of their high hardness values, the ballistic performance of CBN and diamond has long been a question of interest and speculation.

Because of the high costs and manufacturing limitations associated with making bodies predominantly made of either CBN or diamond in sizes large enough for traditional ballistic performance evaluations, it is not surprising that very little has been done in determining their capabilities as armor materials. For CBN, Swab et al.[29] conducted a limited V_{50} conventional ballistic evaluation[30] of a commercially available CBN that was nominally 90 wt% CBN with the rest being made up of aluminum nitride and diboride. The measured Knoop hardness at 2 kgf was approximately 28 GPa.[29] On a thickness basis, this CBN composite ceramic possessed a higher performance than a commercial B_4C; however, on an areal weight† basis, the commercial B_4C was believed to offer equal or slightly superior performance. For diamond, Lundberg et al.[31] determined the fundamental ballistic

* Hardness is used in the context of the "material's intrinsic resistance to inelastic shear deformation" and is therefore an inherent property of the material. Conceptually, this resistance can be inferred qualitatively from hardness values derived from conventional hardness measurement techniques such as Knoop and Vickers. However, because these are dependent upon indenter material and geometry, as well as load, they are not intrinsic properties are therefore, not true measurements of a material's "hardness".

† Areal weight is the system weight per unit area and equals the sum of the system component densities multiplied by their thicknesses.

performance of a synthetic polycrystalline diamond composite (PCD) that contained approximately 11 vol% cobalt (Co). At high pressures and high temperatures (HPHT), Co enables liquid-phase sintering of diamond powders and is a catalyst for new diamond formation during the solution/reprecipitation process.[32–34] Using multiple flash X-rays to elucidate the projectile/target interaction, Lundberg et al.[31] determined the penetration onset velocity for this PCD and several other ceramic materials. The penetration onset velocity for PCD was in the range of 2010–2210 m/s, while for B_4C and SiC, it was in the range of 1430–1480 and 1615–1715 m/s, respectively. Just for reference, the measured Vicker's hardness values for the PCD, B_4C, and SiC were 71, 33, and approximately 22 GPa, respectively. While the studies conducted by Swab et al.[29] and Lundberg et al.[31] were limited in scope, they do reinforce the general notion that higher hardness translates into higher penetration resistance and potentially greater ballistic performance, though other factors such as density, fracture resistance, and target configuration also need consideration.

The lack of ballistic studies on PCD materials is due likely to the pragmatic notion of high cost, limited size, and associated machining challenges that make them impractical for wide application. However, during the last 10–15 years, two situations arose that challenge this perception. The first is that the cost of synthetic diamond grit has dropped steadily and significantly, from dollars to cents per carat* due largely to the scale of China's industrial manufacturing efforts.[35] Based on personal experience and discussions with industry partners, the cost of synthetic diamond grits is now approaching the cost of some armor ceramic powders. The second situation has been the development of low-pressure/high-temperature (LPHT) processing approaches based on reactive metal infiltration for making large PCD bodies driven primarily by thermal management and wear applications.[36–42] In this approach, a porous diamond/SiC skeletal structure is reactively infiltrated with silicon (Si), which also reacts with carbon (C) to form SiC. The resulting SiC fills the interstitial void space of the skeletal structure, thereby producing a fully dense body. This approach overcomes both the cost and size issues that hindered practical considerations of PCDs made by the HPHT process (5–8 GPa, 1500–1700 °C).[32–34] While the diamond contents are not as high as those achievable by the HPHT processing route (90–96 vol%[34]), contents between 20 and 75 vol% have been achieved.[36–42] This is due to the need to preserve reactive metal infiltration pathways within the large porous bodies to ensure complete infiltration. Ideally, the final body will be fully dense, near-net shape, with a microstructure consisting of diamond inclusions embedded in a SiC matrix. Due to the complexities associated with the infiltration, reaction, and graphitization processes,

* 1 gram ≡ 5 carats; 1 lb ≡ 454 grams ≡ 2270 carats.

as well as the evolving nature of the pore channel structure and microstructure, this ideal state is difficult to achieve and some amount of residual Si, non-diamond C, and porosity are practically unavoidable.[37–42] Through optimization of the constituents, constituent composition, particle sizes, binder type and content, and green-pressing pressures, the resulting pore channel structure of the green body and relevant kinetics can be such that these can be minimized. As a result, in addition to their lower cost and large sizes, the exceptional hardness and fracture toughness values of these PCDs,[40–42] make them suitable for ballistic evaluation and potential armor applications.

In the reactive metal infiltration approach, the theoretical limit to diamond content is strongly dependent upon packing of spherical particles.[43–55] For example, for random close-packed arrangement of bimodal-sized spheres, the theoretical limit for the packing efficiency* is approximately 87%.[43–47,53,55] However, practicalities associated with the need to preserve infiltration pathways, minimize graphitization, control reactions, and finite-size differences between powders do play critical roles in determining what is actually possible.†[36–42] As a result, diamond contents up to 60–75 vol% have been produced by this approach.[41,42] Another LPHT approach of interest for making diamond-SiC composites is reactive hot-pressing.[56–58] In this approach, the diamond particulates are mixed together with ceramic and Si powders, and then consolidated to relative densities near 90% of theoretical densities by pressure-assisted sintering at temperatures near the melting point of Si. In principle, the presence of liquid Si would enable particle rearrangement, as well as serve as a liquid-phase sintering medium before being converted into SiC. While little has been done to fully explore this approach for producing ceramic matrix PCDs, it is a potentially viable approach of interest, especially given the high level of expertise in the United States with respect hot-pressing armor ceramics.[59–61] Challenges with graphitization and reactions are similar to those for the reactive infiltration approach; however, additional challenges associated with the elimination of porosity by diffusion processes (i.e., sintering) rather than infiltration are expected.

Fundamentally, the maximum diamond content that is possible with hot-pressing (reactive or conventional) is not known. The maximum diamond content is not expected to be governed by the theoretical limits of particle packing due to the dimensional shrinkage associated with the sintering process. Rather, it is reasoned that the maximum content will be governed by the percolation threshold concept of

* Packing efficiency is the percentage of volume occupied by the particles.

† A materials-by-design approach based on a mesoscale model that incorporates these phenomena with virtual particulate composite bodies would enable understanding of the effects of particle shapes, sizes, and size distributions on the resulting microstructures and properties, as well as guide material development.

percolation theory.[62–66] Percolation theory is a probability-based theory that addresses the formation of long-range connectivity or clustering, as well as the loss of long-range connectivity, in 2-D and 3-D systems characterized by some degree of randomness. Within this theory, the percolation threshold represents the critical condition where long-range connectivity arises or is lost.[62–66] This concept applies to the densification of a particulate system with randomly distributed rigid spherical inclusions in the following manner. During densification, as body dimensions shrink, the distance between inclusions decreases and as it does, contacts between inclusions begin to occur. The number of inclusion-inclusion contacts will increase as densification continues, resulting in the formation of a 3-D inclusion network (i.e., cluster) of subcritical or critical size depending upon the inclusion volume fraction. If the inclusion network size is subcritical, then further densification will occur, but as it does, the size of the network will continue to increase. At the critical size, the inclusion network spans the shrinking dimension and if it is structurally stable and rigid, then densification will cease and the densification limit reached. For this system, the percolation threshold corresponds to the critical volume fraction of inclusions where this dimension-spanning rigid network forms and the body is fully dense. For supercritical inclusion volume fractions, the rigid network forms but the body will only be partially dense, while for subcritical inclusion volume fractions, the body is fully dense, as the rigid network does not form because its size is smaller than the critical size.

For particulate systems with rigid spherical inclusions, two types of percolation thresholds are relevant, 1) conductivity[62–69] and 2) rigidity thresholds.[69–74] The conductivity threshold corresponds to the formation of a continuous conductive path between two surfaces at different electric potential. Strictly speaking, the average inclusion coordination number* (CN) is approximately 2, which is below that necessary for a stable and rigid network. However, for the special condition where the matrix is fully dense, then the network will essentially be both stable and rigid. The rigidity threshold is a more general stability criterion and corresponds to the formation of a rigid network where the average inclusion CN ranges from greater than 2 to 6, with $CN = 6$ representing the most robust rigidity condition for unbounded inclusions because it equals the six linear degrees of freedom.[69–74]

Utilizing the conductivity and rigidity threshold concepts, the purpose of this report is to develop and assess deterministic models for the limits of uniaxial hot-pressing densification of particulate systems with either mono- or bimodal-sized rigid spherical inclusions. Unless stated otherwise, “inclusions” are taken to mean “rigid spherical inclusions”. As presented herein, by considering the randomly distributed

* In this report, the inclusion coordination number is the number of inclusions that each inclusion is in non-bonded contact with.

inclusions in terms of their average spacing along with several other assumptions, simple deterministic models for the maximum or critical volume fraction of mono-sized inclusions and supercritical densification limits can be developed. For bimodal-sized inclusions, a model for only the maximum inclusion volume fraction is developed. Model predictions are assessed by comparing them with percolation threshold models when possible, and experimental data.

2. Deterministic Model Development I: Mono-Sized Inclusions

Consider the idealized representative volume element of the particulate composite body with randomly distributed mono-sized inclusions of diameter D illustrated in Fig. 1. The matrix in which the inclusions are embedded consists of particles of average size d. It is assumed that inclusion size is much greater than the matrix particle size (i.e., $D >> d$). Because of this assumption, the porosity of the composite body is only associated with the particulate matrix. For $D \approx d$, there would be an additional contribution to the porosity associated with the curvature of the inclusions.[46] Therefore, by assuming that $D >> d$, this contribution can be ignored.

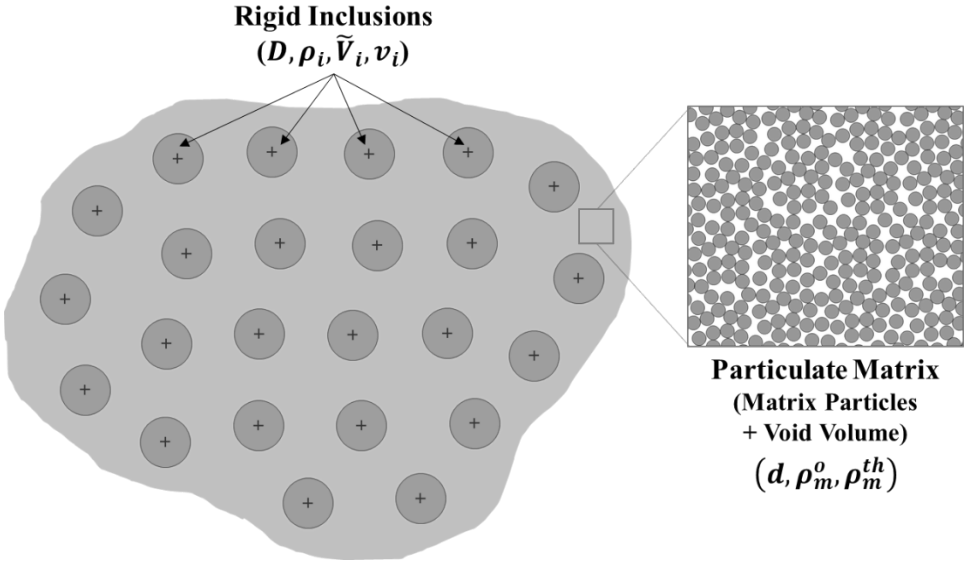

Fig. 1 Schematic illustration of an idealized initial state of a particulate body containing randomly distributed mono-sized inclusions

While the apparent uniformly spaced inclusions depicted in Fig. 1 are strictly not correct in the sense that a finite number of two-inclusion, three-inclusion, and larger inclusion clusters should exist due to increasing finite probabilities of existence with increasing volume fraction, it is still useful conceptually. During densification, the distance between inclusions will shrink primarily in the principal deformation directions. At some point during densification, inclusions will begin to come into

contact with one another leading to the formation of inclusion clusters. These clusters will grow in number and size as densification continues. Eventually, unless complete densification is achieved first, clusters will coalesce, forming a highly connected network of inclusions that spans the shrinking dimensions. Once this happens, if the inclusion network is structurally stable, densification ceases because sintering or applied stresses are unable to overcome the rigidity of the network.

Based on this scenario, the critical or maximum volume fraction of mono-sized inclusions should depend on the initial relative density of the matrix because this determines the average initial spacing of the inclusions, as shown in the following sections. As a note, an attempt was made to keep the amount of math to a level sufficient for the reader to follow the model development if interested.

2.1 Average Inclusion Spacing in the Initially Porous Particulate Composite Body

Prior to densification, the particulate* composite body of initial volume V_o contains N_i inclusions with an initial average spacing L_o (i.e., inclusion center to inclusion center). The concentration of inclusions $\widehat{N}_{V_o}$ (i.e., number of inclusions per unit initial volume) in this initial state is given by

$$\widehat{N}_{V_o} = \frac{N_i}{V_o}$$

For N_i inclusions with an initial average spacing L_o, the initial composite body volume V_o is simply given by

$$V_o = N_i L_o^3$$

Combining these equations yields the following expression for the initial average spacing L_o:

$$L_o = \left(\frac{1}{\widehat{N}_{V_o}}\right)^{\frac{1}{3}} \tag{1}$$

This is not the final expression for the average initial inclusion spacing L_o. The initial concentration of inclusions $\widehat{N}_{V_o}$ can be rewritten into a more useful form in the following manner:

* Particulate composite body is a body composed of discrete particles of two or more phases or compounds and is inherently porous.

$$\widehat{N}_{V_o} = \frac{N_i}{V_o} = \frac{N_i}{V_o} \cdot \frac{\tilde{V}_i}{\tilde{V}_i} \cdot \frac{V_{th}}{V_{th}} = \frac{1}{\tilde{V}_i} \cdot \frac{N_i \tilde{V}_i}{V_{th}} \cdot \frac{V_{th}}{V_o} \Longrightarrow \widehat{N}_{V_o} = \frac{1}{\tilde{V}_i} \cdot \frac{V_i}{V_{th}} \cdot \frac{V_{th}}{V_o}$$

Here $\tilde{V}_i$ is the volume of a single inclusion, V_i is the total volume of inclusions ($V_i = N_i \tilde{V}_i$), and V_{th} is the volume of the fully dense composite body. This expression can be rewritten further as

$$\widehat{N}_{V_o} = \frac{1}{\tilde{V}_i} \cdot \frac{V_i}{V_{th}} \cdot \frac{V_{th}}{V_o} = \frac{6}{\pi D^3} \cdot v_i \cdot \frac{\rho_o}{\rho_{th}} = \frac{6 v_i}{\pi D^3} \left(\frac{\rho_o}{\rho_{th}} \right)$$

where v_i is the volume fraction of inclusions, ρ_o is the initial particulate composite body density, and ρ_{th} is the theoretical density of the composite body. The conservation of mass expression $\frac{V_{th}}{V_o} = \frac{\rho_o}{\rho_{th}}$ and $\tilde{V}_i = \frac{1}{6}\pi D^3$ were used in deriving this expression. Therefore, the initial average inclusion spacing L_o normalized to the inclusion diameter *D*:

$$\frac{L_o}{D} = \left[\frac{\pi}{6 v_i} \left(\frac{\rho_{th}}{\rho_o} \right) \right]^{\frac{1}{3}} \tag{2}$$

Equation 2 is still not the final form because the initial density of the particulate composite body can be expressed in terms of the inclusion volume fraction and the relative initial density of the matrix as is shown next.

2.2 Initial Density of the Particulate Composite Body

The particulate composite body is characterized by its initial density ρ_o, which is dependent upon the volume fraction v_i of inclusions, the density ρ_i of the inclusions, and the initial density ρ_m^o of the matrix. Using the rule-of-mixtures, ρ_o is expressed in terms of the inclusion and matrix volume fractions:

$$\rho_o = \left(\frac{V_i}{V_o} \right) \rho_i + \left(\frac{V_m^o}{V_o} \right) \rho_m^o$$

where V_m^o is the volume of the porous matrix. From a processing viewpoint, it is most convenient to reference the volume fraction of inclusions to the fully dense state rather than the initial porous state. Using the fact that $V_o = V_i + V_m^o$ and $v_i = \frac{V_i}{V_{th}}$ the previous equation can be rewritten as

$$\rho_o = \rho_m^o + v_i \left(\frac{V_{th}}{V_o} \right) (\rho_i - \rho_m^o)$$

Substitution of conservation of mass expression $\frac{V_{th}}{V_o} = \frac{\rho_o}{\rho_{th}}$ into this equation yields

$$\frac{\rho_o}{\rho_{th}} = \frac{\rho_m^o}{\rho_{th} - (\rho_i - \rho_m^o)v_i}$$

The theoretical density ρ_{th} can be written in the following form based on the rule of mixtures and $v_i + v_m^{th} = 1$:

$$\rho_{th} = v_i\rho_i + v_m^{th}\rho_m^{th} = \rho_m^{th} + (\rho_i - \rho_m^{th})v_i$$

where v_m^{th} and ρ_m^{th} are the volume fraction of the fully dense matrix and theoretical density of the matrix, respectively. Substituting this expression into the previous equation yields the final form for the initial relative density of the particulate composite body:

$$\frac{\rho_o}{\rho_{th}} = \frac{\frac{\rho_m^o}{\rho_m^{th}}}{1-\left(1-\frac{\rho_m^o}{\rho_m^{th}}\right)v_i} \tag{3}$$

Equation 3 is shown plotted in Fig. 2 for initial relative matrix densities of 0.4, 0.5, and 0.6. As expected, the higher the initial matrix density, the higher the initial particulate composite density with increasing inclusion volume fraction.

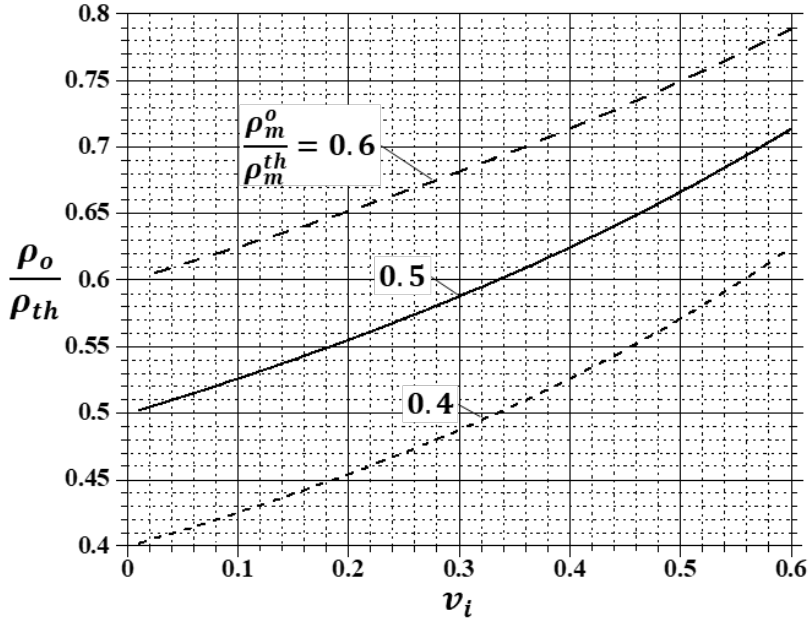

Fig. 2 Variation of relative initial composite density as a function of inclusion volume fraction and initial relative matrix densities

For completeness, substituting Eq. 3 into Eq. 2 and rearranging yields the explicit relationship between the initial average relative inclusion spacing $\frac{L_o}{D}$ in terms of the volume fraction of inclusions and initial relative matrix density:

$$\frac{L_o}{D} = \left\{\frac{\pi}{6v_i}\left(\frac{\rho_m^{th}}{\rho_m^o}\right)\left[1-\left(1-\frac{\rho_m^o}{\rho_m^{th}}\right)v_i\right]\right\}^{\frac{1}{3}} \tag{4}$$

The initial average relative inclusion spacing is shown in Fig. 3 for the initial relative matrix densities shown in Fig. 2. It appears that the initial average relative inclusion spacing is a strong function of inclusion volume fraction but not initial relative matrix density. But as shown next, it does have a strong effect on the densification limit.

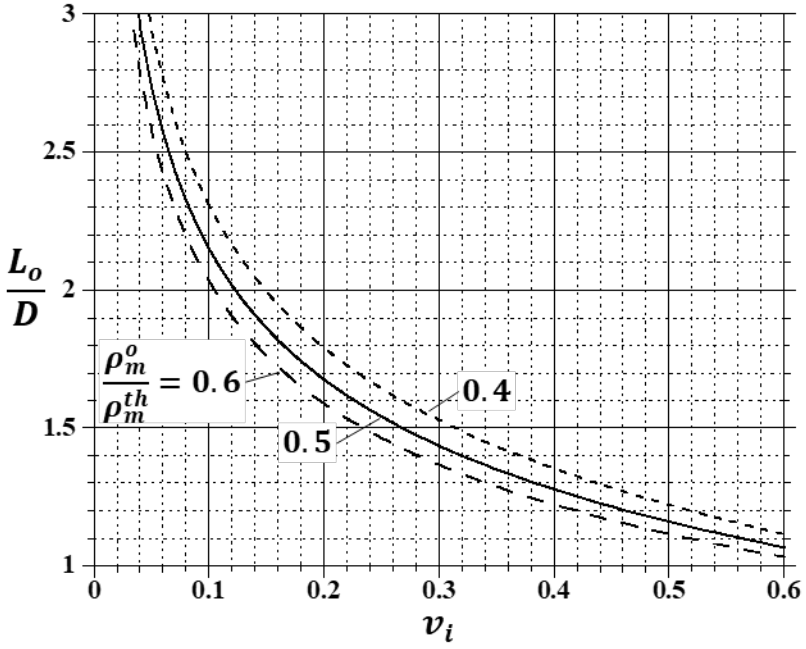

Fig. 3 Initial average relative inclusion spacing as a function of inclusion volume fraction and initial relative matrix densities

2.3 Densification/Inclusion Spacing Relationship

For the cylindrical body shown in Fig. 4 undergoing uniaxial shrinkage such as experienced in uniaxial hot-pressing, the density of the cylinder during shrinkage is simply determined from the conservation of mass and is given by

$$\frac{\rho}{\rho_o} = \frac{V_o}{V} = \frac{A_o h_o}{A_o h} = \frac{h_o}{h}$$

where h_o and h are the initial and instantaneous cylinder heights, respectively. Note that for conventional hot-pressing, the body diameter remains essentially constant. From this expression, the instantaneous relative density is given by

$$\frac{\rho}{\rho_{th}} = \frac{h_o}{h} \cdot \frac{\rho_o}{\rho_{th}}$$

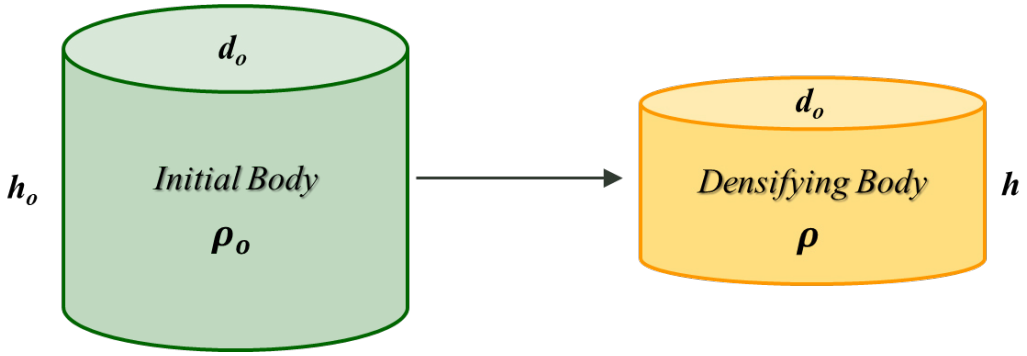

Fig. 4 Porous cylindrical body of initial height h_o and density ρ_o undergoing uniaxial shrinkage similar to that experienced during uniaxial hot-pressing. The current state of the porous cylindrical body is indicated by its instantaneous height h and corresponding density ρ.

The instantaneous cylinder height h is related to the average inclusion spacing in the direction of shrinkage by $h = N_{h_o} L$ where N_{h_o} is the average number of inclusions in the height direction of the initially porous cylindrical body and L is the instantaneous average inclusion spacing in the height direction. Substitution of this relationship into the previous expression yields

$$\frac{\rho}{\rho_{th}} = \frac{L_o}{L} \cdot \frac{\rho_o}{\rho_{th}} = \frac{L_o/D}{L/D} \cdot \frac{\rho_o}{\rho_{th}}$$

Substituting Eqs. 3 and 4 into this expression yields the most useful form for the densification/inclusion spacing relationship:

$$\frac{\rho}{\rho_{th}} = \frac{1}{L/D}\left(\frac{\pi}{6v_i}\right)^{\frac{1}{3}}\left[\frac{\frac{\rho_m^o}{\rho_m^{th}}}{1-\left(1-\frac{\rho_m^o}{\rho_m^{th}}\right)v_i}\right]^{\frac{2}{3}} \tag{5}$$

The instantaneous relative particulate composite density ρ/ρ_{th} is a function of the relative instantaneous inclusion spacing L/D, the volume fraction of inclusions v_i, and the relative initial density of the matrix ρ_m^o/ρ_m^{th}. From this equation, the critical

volume fraction of mono-sized inclusions and supercritical densification limit for the conductivity and rigidity threshold models will be determined.

2.4 Conductivity Threshold Model

During densification, the average inclusion spacing in the pressing direction decreases as depicted in Fig. 5. Perpendicular to the pressing direction, the average inclusion spacing does not change. The critical condition occurs when the spacing of the inclusions decreases to the inclusion diameter D and the inclusions are touching in the pressing direction. As mentioned previously, the critical condition depicted in Fig. 5c corresponds to the "conductivity" threshold, which is analogous to the percolation problem of conducting particles embedded in an insulating matrix forming a conductive path connecting two surfaces of differing electrical potential at a critical volume fraction of conducting particles.[62–69] The critical volume fraction of inclusions v_i^{C*} corresponds to the condition $L = D$ and $\rho = \rho_{th}$ in Eq. 5. With these conditions, Eq. 5 yields the following cubic equation for v_i^C:

$$v_i^{c\,3} - \left(\frac{2}{1-\frac{\rho_m^o}{\rho_m^{th}}}\right) v_i^{c\,2} + \left(\frac{1}{1-\frac{\rho_m^o}{\rho_m^{th}}}\right)^2 v_i^c - \frac{\pi}{6}\left(\frac{\frac{\rho_m^o}{\rho_m^{th}}}{1-\frac{\rho_m^o}{\rho_m^{th}}}\right)^2 = 0 \qquad (6)$$

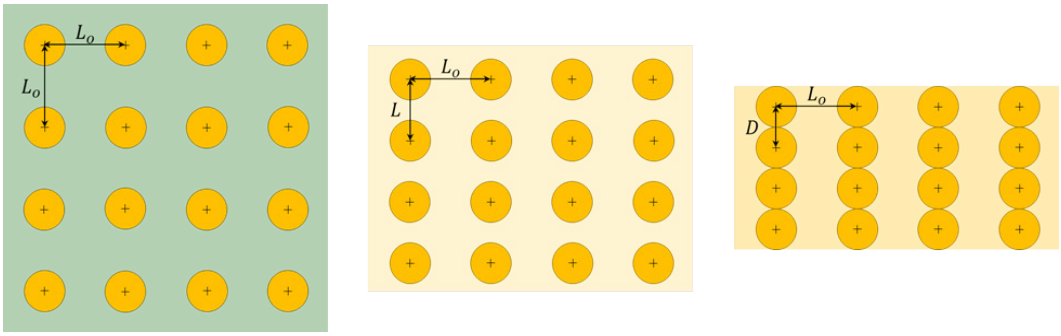

(a) **(b)** **(c)**

Fig. 5 Schematic illustration of the state of the "microstructure" as various moments in time: a) initial state, b) instantaneous state, and c) final or conductivity threshold state

* Superscript "C" denotes conductivity threshold condition.

A general explicit relationship for v_i^C can be written by solving Eq. 6; however, the analytical solution is relatively cumbersome and will not be pursued here. If the cubic term is negligible relative to the other terms, an approximate solution is easily obtained:

$$v_i^C \cong \frac{1}{4}\left(\frac{1}{1-\frac{\rho_m^o}{\rho_m^{th}}}\right)\left[1-\sqrt{1-\frac{4\pi}{3}\left(1-\frac{\rho_m^o}{\rho_m^{th}}\right)\left(\frac{\rho_m^o}{\rho_m^{th}}\right)^2}\right] \tag{7}$$

Numerical solutions to Eqs. 6 and 7 are plotted in Fig. 6 as a function of the initial relative matrix density $\frac{\rho_m^o}{\rho_m^{th}}$. As can be seen, Eq. 7 is an excellent approximate solution to Eq. 6. As anticipated, the critical inclusion volume fraction is higher for higher initial relative matrix densities. This is because less height change is required to achieve full density. Consequently, inclusions can initially be more closely spaced within of the particulate composite body, which corresponds to higher inclusion concentrations.

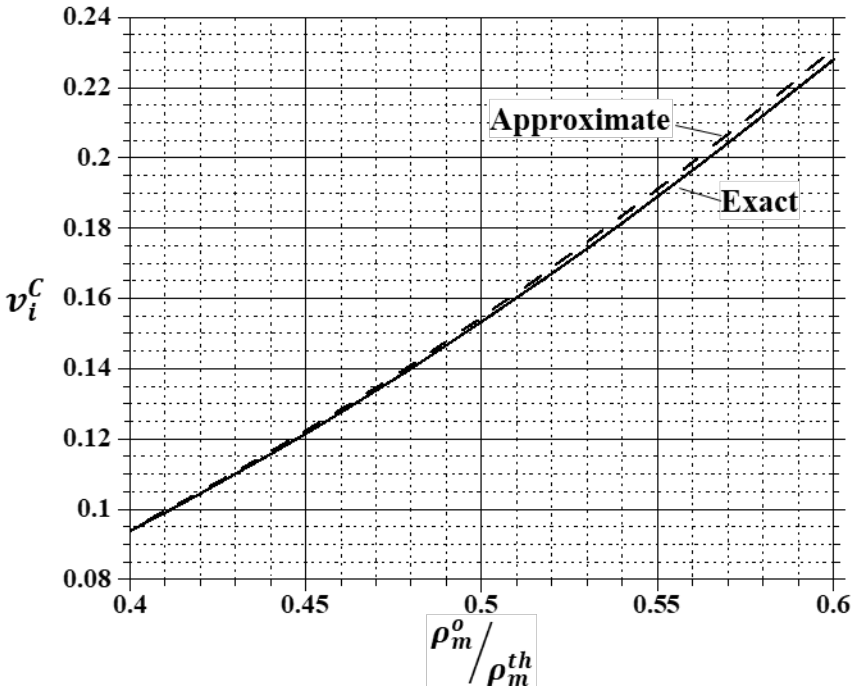

Fig. 6 Conductivity threshold model predictions for the maximum or critical inclusion volume fraction variation with initial relative matrix density based on numerical solutions to Eq. 6 and approximate solution given by Eq. 7

For supercritical inclusion volume fractions (i.e., $v_i \geq v_i^C$), the maximum or limit composite density ρ_{limit}^C given by Eq. 5 with $L = D$, is going to be less than 1. The limit composite density ρ_{limit}^C is given by

$$\frac{\rho_{limit}^{C}}{\rho_{th}} = \left\{ \frac{\pi}{6v_i} \left[\frac{\frac{\rho_m^o}{\rho_m^{th}}}{1-\left(1-\frac{\rho_m^o}{\rho_m^{th}}\right)v_i} \right]^2 \right\}^{\frac{1}{3}} \tag{8}$$

This is shown plotted in Fig. 7 for several $\frac{\rho_m^o}{\rho_m^{th}}$ values. As can be seen, the initial relative matrix density has a significant effect on the relative composite density limit for a given supercritical inclusion volume fraction.

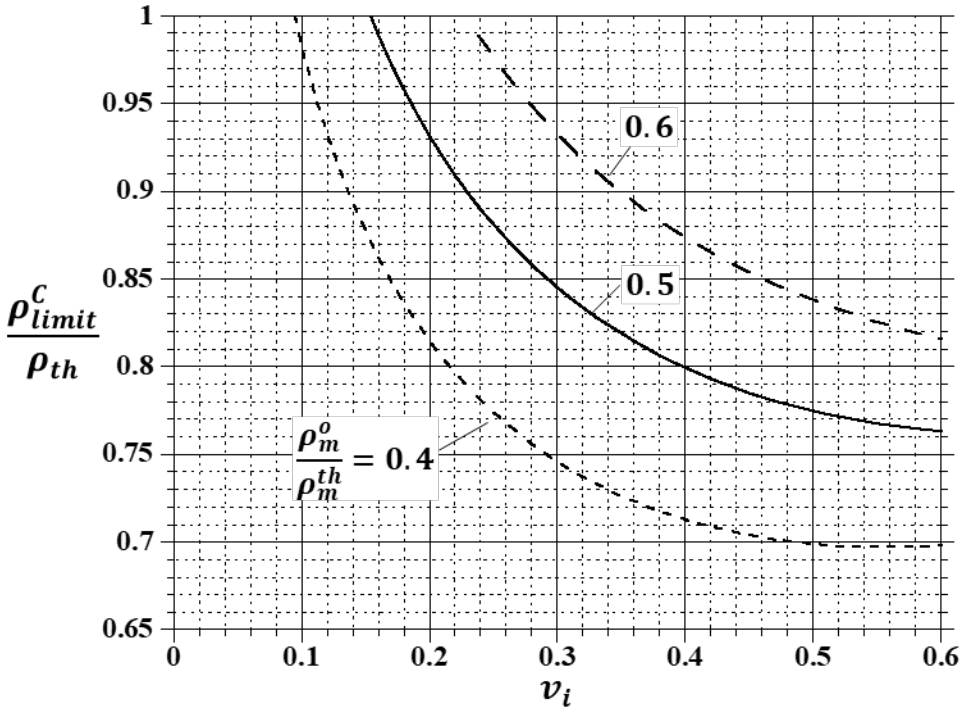

Fig. 7 Supercritical densification limits for the relative composite density limits for $v_i \geq v_i^C$ and several values for the initial relative matrix density

2.5 Rigidity Threshold Model

For the conductive threshold configuration depicted in Fig. 8a, the CN for each inclusion is only 2. Because this is less than the total number of degrees of freedom for each inclusion (i.e., 6) ignoring rotational degrees of freedom, the configuration is only stable if the matrix is fully dense or if the inclusions are bonded to one another. Therefore, if either condition is not met, then the configuration is unstable because local shear stresses may exceed frictional contact stresses between inclusions allowing them to shift and rearrange. This allows further densification to occur as depicted in Fig. 8b. Once the matrix reaches full density or a more stable inclusion network configuration is attained, densification ceases as depicted in

Fig. 8c. In principle, the most stable configurations will be when the inclusion $CN \geq 6$, such that the constraints on each inclusion equals or exceeds the six linear degrees of freedom (i.e., x-y-z). However, a fairly stable intermediate inclusion network configuration is the diamond cubic structure where the maximum $CN = 4$. This structure is illustrated in Fig. 9a. As shown in Fig. 9b, each inclusion essentially sits within a tetrahedron at a point that is equidistant from four other inclusions located at the four corners or vertices of the tetrahedron. As the distance between inclusions shrinks during densification, the central inclusion will become constrained on the top, bottom, and sides by the four other inclusions, resulting in metastable equilibrium configuration with a high degree of rigidity. In this model, it is assumed that the inclusions will rearrange into this intermediate metastable configuration. The rigidity threshold corresponds to the condition where the matrix reaches full density and the $CN \approx 4$. It should be evident from this discussion that the critical inclusion volume fraction v_i^{R*} for the rigidity threshold will be greater than v_i^C.

The development of the rigidity threshold model is more math intensive than that for the conductivity threshold model. However, efforts are made to keep the math to a level where it is easy to follow if the reader desires.

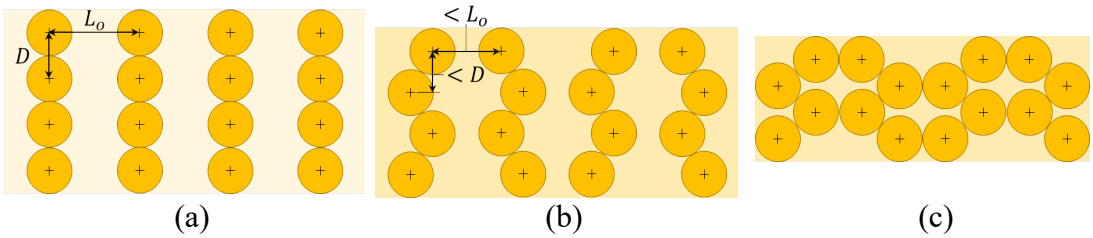

Fig. 8 Schematic illustration of depicting the possibility for inclusion rearrangement when a) the matrix is not fully dense when the inclusions first touch, b) intermediate stage or matrix has achieved full density, and c) rigid threshold condition

[*] Superscript "R" denotes rigidity threshold condition.

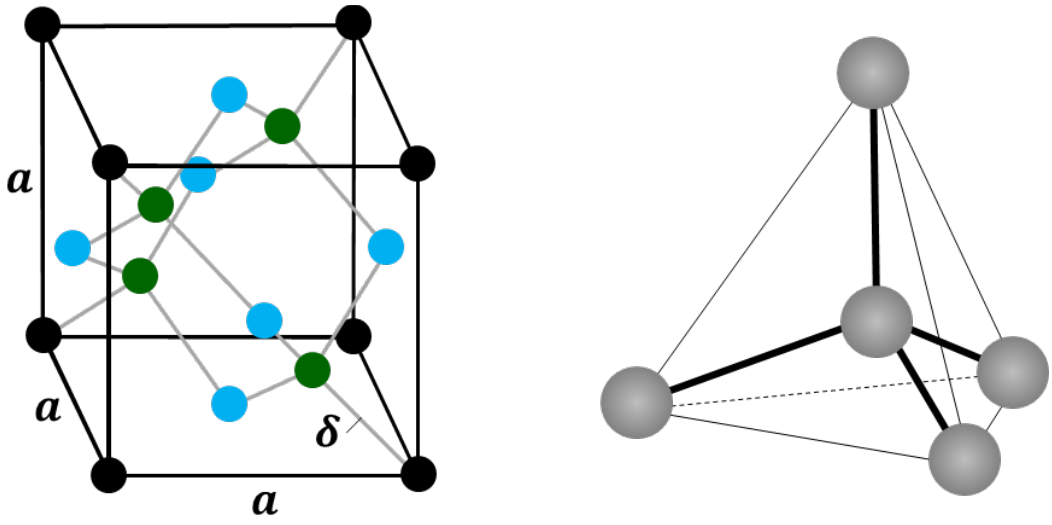

(a) (b)

Fig. 9 a) Diamond cubic structure with cell size a and sphere spacing = δ. Corner spheres: black; face-centered spheres: blue; and interior spheres: green. b) Tetrahedral coordination for each inclusion.

2.5.1 Initial Inclusion Spacing

The initial inclusion spacing δ_o for the diamond cubic structure shown in Fig. 9a is determined from its initial cell volume V_o^R, which is related to the cell volume V^C of the conductivity threshold structure. From the conservation of mass, the initial volume per inclusion $\hat{V}_o^R$ for the diamond cubic structure and that corresponding to the conductivity threshold structure are equal.

For the diamond cubic structure, the number of inclusions per unit cell is designated as N_i^R, while that for the conductivity threshold structure is designated as N_i^C. Therefore, it follows that

$$\hat{V}_o^R = \frac{V_o^R}{N_i^R} = \hat{V}^C = \frac{V^C}{N_i^C} \Rightarrow V_o^R = \left(\frac{N_i^R}{N_i^C}\right) V^C = a_o^3$$

$$a_o = \left[\left(\frac{N_i^R}{N_i^C}\right) V^C\right]^{\frac{1}{3}}$$

where a_o is the initial characteristic size of the diamond cubic cell shown in Fig. 9a. For the diamond cubic cell $N_i^R = 8$, while for the conductivity threshold structure cell $N_i^C = 1$ and $V^C = DL_o^2$. Substitution into the previous expression yields the following equation for the initial characteristic size a_o of the diamond cubic cell:

$$a_o = (8DL_o^2)^{\frac{1}{3}} = 2\left(D^3\frac{L_o^2}{D^2}\right)^{\frac{1}{3}} = 2D\left(\frac{L_o}{D}\right)^{\frac{2}{3}}$$

$$= 2D\left(\left\{\frac{\pi}{6v_i}\left(\frac{\rho_m^{th}}{\rho_m^o}\right)\left[1-\left(1-\frac{\rho_m^o}{\rho_m^{th}}\right)v_i\right]\right\}^{\frac{1}{3}}\right)^{\frac{2}{3}}$$

$$a_o = 2D\left\{\frac{\pi}{6v_i}\left(\frac{\rho_m^{th}}{\rho_m^o}\right)\left[1-\left(1-\frac{\rho_m^o}{\rho_m^{th}}\right)v_i\right]\right\}^{\frac{2}{9}} \tag{9}$$

where $\frac{L_o}{D}$ is given by Eq. 4 with $v_i \geq v_i^C$. The initial inclusion spacing δ_o is related to a_o by the following relation:

$$\delta_o = \frac{\sqrt{3}}{4}a_o = \frac{\sqrt{3}}{4}\cdot 2D\left\{\frac{\pi}{6v_i}\left(\frac{\rho_m^{th}}{\rho_m^o}\right)\left[1-\left(1-\frac{\rho_m^o}{\rho_m^{th}}\right)v_i\right]\right\}^{\frac{2}{9}}$$

$$\delta_o = \frac{\sqrt{3}}{2}D\left\{\frac{\pi}{6v_i}\left(\frac{\rho_m^{th}}{\rho_m^o}\right)\left[1-\left(1-\frac{\rho_m^o}{\rho_m^{th}}\right)v_i\right]\right\}^{\frac{2}{9}} \tag{10}$$

Equation 10 is shown plotted in Fig. 10 as a function of inclusion volume fraction v_i for several values for the initial relative matrix density $\frac{\rho_m^o}{\rho_m^{th}}$. The starting values for v_i for each value of $\frac{\rho_m^o}{\rho_m^{th}}$ were obtained from Fig. 6 or given approximately by Eq. 7.

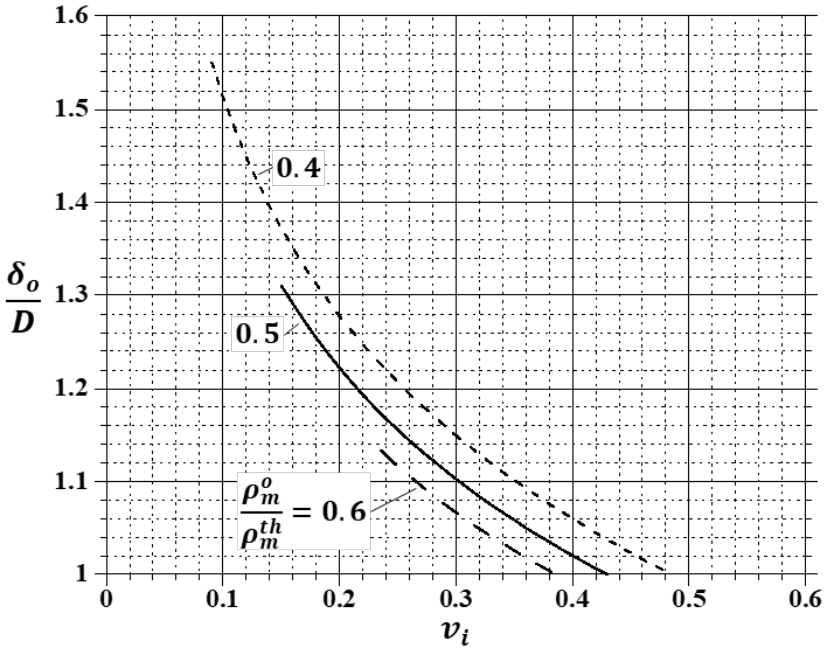

Fig. 10 Variation of initial relative inclusion spacing with inclusion volume fraction and several values for the initial relative matrix density

2.5.2 Supercritical Densification Limit

The limit of densification is achieved when the inclusions are touching (i.e., $\delta \cong D$) in the hot-pressing direction, yielding a characteristic cell height $a^R \cong \frac{4}{\sqrt{3}}D$. The unit cell volume V^R when this condition occurs is given by

$$V^R = a^R a_o^2 = \frac{4}{\sqrt{3}} D \cdot \left[2D \left\{ \frac{\pi}{6v_i} \left(\frac{\rho_m^{th}}{\rho_m^o} \right) \left[1 - \left(1 - \frac{\rho_m^o}{\rho_m^{th}} \right) v_i \right] \right\}^{\frac{2}{9}} \right]^2$$

$$V^R = \frac{16}{\sqrt{3}} D^3 \left\{ \frac{\pi}{6v_i} \left(\frac{\rho_m^{th}}{\rho_m^o} \right) \left[1 - \left(1 - \frac{\rho_m^o}{\rho_m^{th}} \right) v_i \right] \right\}^{\frac{4}{9}} \tag{11}$$

To calculate the additional densification that is possible as a result of the rearrangement of inclusions into the diamond cubic structure, the conservation of mass is used:

$$\frac{\rho_{limit}^R}{\rho_{limit}^C} = \frac{\hat{V}^C}{\hat{V}^R} = \frac{N_i^R V^C}{N_i V^R} = \frac{8DL_o^2}{V^R} = \frac{8D^3}{V^R} \left(\frac{L_o}{D} \right)^2$$

$$= \frac{8D^3\left\{\frac{\pi}{6v_i}\left(\frac{\rho_m^{th}}{\rho_m^o}\right)\left[1-\left(1-\frac{\rho_m^o}{\rho_m^{th}}\right)v_i\right]\right\}^{\frac{2}{3}}}{\frac{16}{\sqrt{3}}D^3\left\{\frac{\pi}{6v_i}\left(\frac{\rho_m^{th}}{\rho_m^o}\right)\left[1-\left(1-\frac{\rho_m^o}{\rho_m^{th}}\right)v_i\right]\right\}^{\frac{4}{9}}} = \frac{\sqrt{3}}{2}\left\{\frac{\pi}{6v_i}\left(\frac{\rho_m^{th}}{\rho_m^o}\right)\left[1-\left(1-\frac{\rho_m^o}{\rho_m^{th}}\right)v_i\right]\right\}^{\frac{2}{9}}$$

$$\frac{\rho_{limit}^R}{\rho_{th}} = \frac{\sqrt{3}}{2}\left\{\frac{\pi}{6v_i}\left(\frac{\rho_m^{th}}{\rho_m^o}\right)\left[1-\left(1-\frac{\rho_m^o}{\rho_m^{th}}\right)v_i\right]\right\}^{\frac{2}{9}}\left(\frac{\rho_{limit}^C}{\rho_{th}}\right)$$

where $\frac{\rho_{limit}^C}{\rho_{th}}$ is given by Eq. 8. Substitution of Eq. 8 yields

$$\frac{\rho_{limit}^R}{\rho_{th}} = \frac{\sqrt{3}}{2}\left\{\frac{\pi}{6v_i}\left(\frac{\rho_m^{th}}{\rho_m^o}\right)\left[1-\left(1-\frac{\rho_m^o}{\rho_m^{th}}\right)v_i\right]\right\}^{\frac{2}{9}}\left\{\frac{\pi}{6v_i}\left[\frac{\frac{\rho_m^o}{\rho_m^{th}}}{1-\left(1-\frac{\rho_m^o}{\rho_m^{th}}\right)v_i}\right]^2\right\}^{\frac{1}{3}}$$

$$= \frac{\sqrt{3}}{2}\left\{\frac{\pi}{6v_i}\left(\frac{\rho_m^{th}}{\rho_m^o}\right)\left[1-\left(1-\frac{\rho_m^o}{\rho_m^{th}}\right)v_i\right]\right\}^{\frac{2}{9}}\left\{\frac{\pi}{6v_i}\left[\frac{\frac{\rho_m^o}{\rho_m^{th}}}{1-\left(1-\frac{\rho_m^o}{\rho_m^{th}}\right)v_i}\right]^2\right\}^{\frac{3}{9}}$$

$$= \frac{\sqrt{3}}{2}\left(\frac{\pi}{6v_i}\right)^{\frac{2}{9}}\left(\frac{\rho_m^{th}}{\rho_m^o}\right)^{\frac{2}{9}}\left[1-\left(1-\frac{\rho_m^o}{\rho_m^{th}}\right)v_i\right]^{\frac{2}{9}}\left\{\frac{\left(\frac{\pi}{6v_i}\right)^{\frac{3}{9}}\left(\frac{\rho_m^o}{\rho_m^{th}}\right)^{\frac{6}{9}}}{\left[1-\left(1-\frac{\rho_m^o}{\rho_m^{th}}\right)v_i\right]^{\frac{6}{9}}}\right\}$$

$$= \frac{\sqrt{3}}{2}\left(\frac{\pi}{6v_i}\right)^{\frac{2}{9}}\left(\frac{\pi}{6v_i}\right)^{\frac{3}{9}}\left(\frac{\rho_m^{th}}{\rho_m^o}\right)^{\frac{2}{9}}\left(\frac{\rho_m^o}{\rho_m^{th}}\right)^{\frac{6}{9}}\frac{\left[1-\left(1-\frac{\rho_m^o}{\rho_m^{th}}\right)v_i\right]^{\frac{2}{9}}}{\left[1-\left(1-\frac{\rho_m^o}{\rho_m^{th}}\right)v_i\right]^{\frac{6}{9}}}$$

$$\frac{\rho_{limit}^R}{\rho_{th}} = \frac{\frac{\sqrt{3}}{2}\left(\frac{\rho_m^o}{\rho_m^{th}}\right)^{\frac{4}{9}}\left(\frac{\pi}{6v_i}\right)^{\frac{5}{9}}}{\left[1-\left(1-\frac{\rho_m^o}{\rho_m^{th}}\right)v_i\right]^{\frac{4}{9}}} \qquad (12)$$

Equation 12 relates the limit relative composite density $\frac{\rho_{limit}^{R}}{\rho_{th}}$ to the initial relative matrix density $\frac{\rho_m^o}{\rho_m^{th}}$ and volume fraction of inclusions v_i ($v_i \geq v_i^C$).

2.5.3 Rigidity Threshold

At the rigidity threshold condition in Eq. 12 $\rho_{limit}^{R} = \rho_{th}$ and $v_i = v_i^R$. This condition results in the following equation for v_i^R:

$$v_i^{R\,5}\left[1-\left(1-\frac{\rho_m^o}{\rho_m^{th}}\right)v_i^R\right]^4 = \left(\frac{\pi}{6}\right)^5\left(\frac{\sqrt{3}}{2}\right)^9\left(\frac{\rho_m^o}{\rho_m^{th}}\right)^4 \tag{13}$$

As for the conductivity threshold model, an exact analytical solution for v_i^R in terms of $\frac{\rho_m^o}{\rho_m^{th}}$ can be derived from Eq. 13. Because of the magnitude of the exponents involved, this is very difficult and is not pursued here. As before, for specific $\frac{\rho_m^o}{\rho_m^{th}}$ values, corresponding v_i^R can easily be calculated numerically. While a practical approach, it is less elegant mathematically. By careful consideration of the terms and exponents in Eq. 13, an approximate analytical solution for v_i^R can be derived in the following manner:

$$v_i^{R\,5}\left[1-\left(1-\frac{\rho_m^o}{\rho_m^{th}}\right)v_i^R\right]^4 = \left(\frac{\pi}{6}\right)^5\left(\frac{\sqrt{3}}{2}\right)^9\left(\frac{\rho_m^o}{\rho_m^{th}}\right)^4$$

$$v_i^{R\,5}\left[1-\left(1-\frac{\rho_m^o}{\rho_m^{th}}\right)v_i^R\right]^5 = \left(\frac{\pi}{6}\right)^5\left(\frac{\sqrt{3}}{2}\right)^9\left(\frac{\rho_m^o}{\rho_m^{th}}\right)^4\left[1-\left(1-\frac{\rho_m^o}{\rho_m^{th}}\right)v_i^R\right]$$

$$v_i^R\left[1-\left(1-\frac{\rho_m^o}{\rho_m^{th}}\right)v_i^R\right] = \frac{\pi}{6}\left(\frac{\sqrt{3}}{2}\right)^{\frac{9}{5}}\left(\frac{\rho_m^o}{\rho_m^{th}}\right)^{\frac{4}{5}}\left[1-\left(1-\frac{\rho_m^o}{\rho_m^{th}}\right)v_i^R\right]^{\frac{1}{5}}$$

$$v_i^R\left[1-\left(1-\frac{\rho_m^o}{\rho_m^{th}}\right)v_i^R\right] \cong \frac{\pi}{6}\left(\frac{\sqrt{3}}{2}\right)^{\frac{9}{5}}\left(\frac{\rho_m^o}{\rho_m^{th}}\right)^{\frac{4}{5}}\left[1-\frac{1}{5}\left(1-\frac{\rho_m^o}{\rho_m^{th}}\right)v_i^R\right]$$

where the term $\left[1-\left(1-\frac{\rho_m^o}{\rho_m^{th}}\right)v_i^R\right]^{\frac{1}{5}}$ was approximated by the first and second terms in its Taylor series expansion. Expanding this equation and rearranging terms results in the following quadratic equation for v_i^R:

$$\left(1-\frac{\rho_m^o}{\rho_m^{th}}\right)v_i^{R\,2}-\left[1+\frac{\pi}{30}\left(\frac{\sqrt{3}}{2}\right)^{\frac{9}{5}}\left(1-\frac{\rho_m^o}{\rho_m^{th}}\right)\left(\frac{\rho_m^o}{\rho_m^{th}}\right)^{\frac{4}{5}}\right]v_i^R+\frac{\pi}{6}\left(\frac{\sqrt{3}}{2}\right)^{\frac{9}{5}}\left(\frac{\rho_m^o}{\rho_m^{th}}\right)^{\frac{4}{5}}\cong 0 \tag{14}$$

which has the following simple solution:

$$v_i^R\cong\frac{1}{2\left(1-\frac{\rho_m^o}{\rho_m^{th}}\right)}\left[1+\frac{\pi}{30}\left(\frac{\sqrt{3}}{2}\right)^{\frac{9}{5}}\left(1-\frac{\rho_m^o}{\rho_m^{th}}\right)\left(\frac{\rho_m^o}{\rho_m^{th}}\right)^{\frac{4}{5}}-\sqrt{\left[1+\frac{\pi}{30}\left(\frac{\sqrt{3}}{2}\right)^{\frac{9}{5}}\left(1-\frac{\rho_m^o}{\rho_m^{th}}\right)\left(\frac{\rho_m^o}{\rho_m^{th}}\right)^{\frac{4}{5}}\right]^2-\frac{2\pi}{3}\left(\frac{\sqrt{3}}{2}\right)^{\frac{9}{5}}\left(1-\frac{\rho_m^o}{\rho_m^{th}}\right)\left(\frac{\rho_m^o}{\rho_m^{th}}\right)^{\frac{4}{5}}}\right] \tag{15}$$

Equation 15 is plotted in Fig. 11 along with numerically calculated values determined by the iterative approach. As can be seen, the approximate solution is in excellent agreement with numerically calculated values to Eq. 13. As expected, the critical inclusion volume fraction values are higher than the corresponding values predicted by the conductivity threshold model shown in Fig. 6.

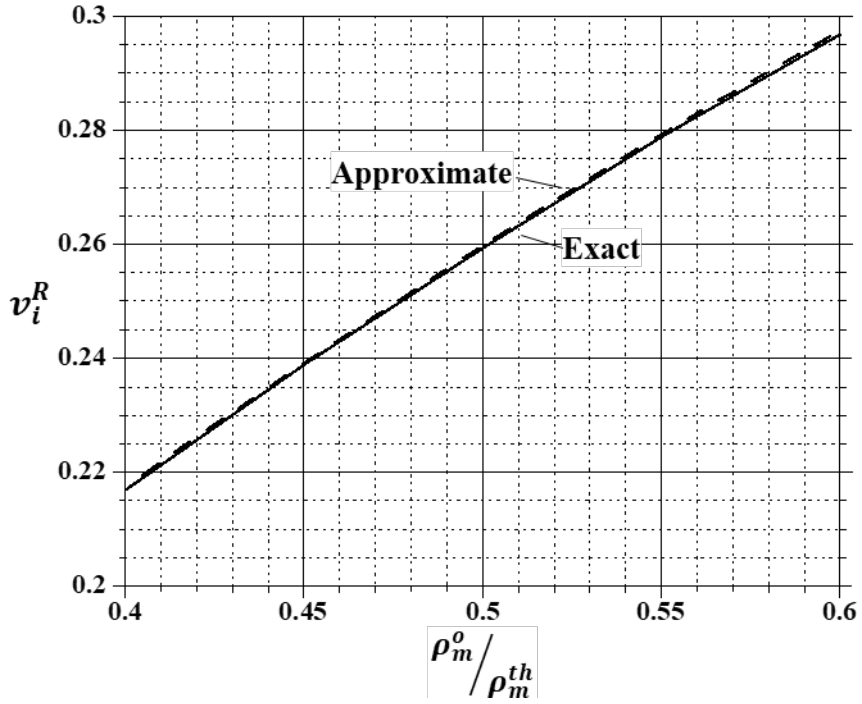

Fig. 11 Rigidity threshold model predictions for the maximum or critical volume fraction of inclusions variation with initial relative matrix density based on numerical solutions to Eq. 13 and approximate solutions given by Eq. 15

For supercritical inclusion volume fractions (i.e., $v_i \geq v_i^R$), the maximum relative density will be less than 1 and is given by Eq. 12. This is plotted in Fig. 12 as a function of v_i and several $\frac{\rho_m^o}{\rho_m^{th}}$ values. As with the conductivity threshold model, the rigidity threshold model supercritical density predictions are very sensitive to initial relative matrix density.

Both the critical inclusion volume fraction and supercritical limit density predictions of the conductivity and rigidity threshold models were used to guide experimentation in an effort to validate these predictions. Before assessing these predictions based on comparison with experimental data, a model for the case of the densification of a particulate composite with bimodal-sized inclusions by uniaxial hot-pressing will be developed. The development of this model is surprisingly simple and is based on a key assumption independently arrived at but exercised by Furnas[43] almost a century before.

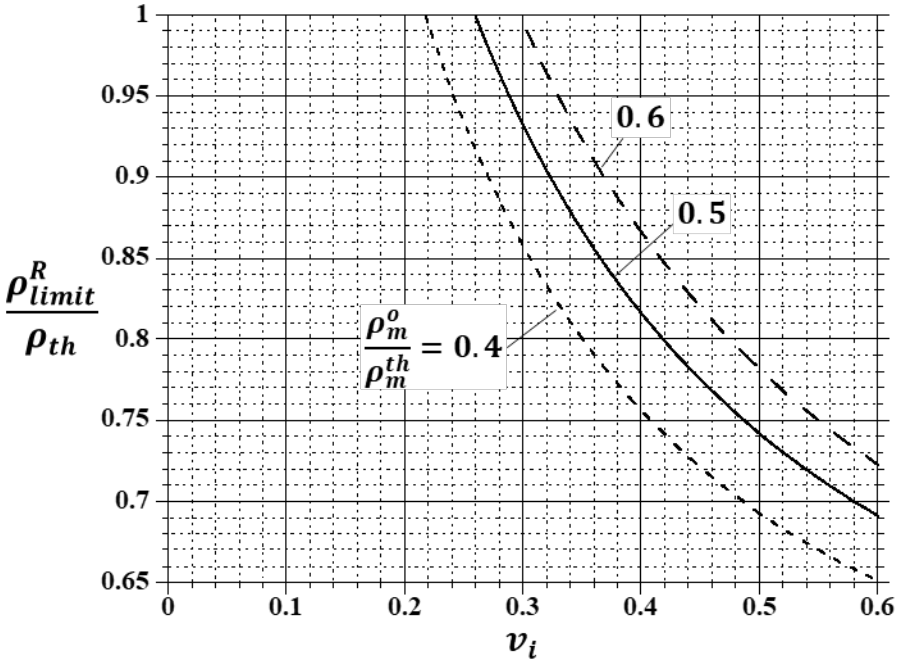

Fig. 12 Supercritical densification limits for the relative composite density for $v_i \geq v_i^R$ and several values for the initial relative matrix density

3. Deterministic Model Development II: Bimodal-Sized Inclusions

The key assumption to developing a threshold hold model for a particulate composite body with bimodal-sized inclusions is that the large inclusion size is much larger than the small inclusion size, which is much larger than the matrix particle size. Mathematically, this can be expressed as $D_{large} \gg D_{small} \gg d$ or $D_{large}/D_{small} \to \infty$ and $D_{small}/d \to \infty$. This greatly reduces the complexity of the analyses by allowing the effects of finite size differences between the large and small spheres or inclusions and matrix particles to be ignored. This is the assumption that Furnas[43] used nearly a century ago for estimating the upper limit to the packing efficiency* for bimodal-sized random close-packed spheres.

For random close-packing of bimodal-sized spheres, the concept is shown in the inset images within Fig. 13,[55] which is also a plot of the packing efficiency as a function of the fraction f of packing efficiency that is made up by the smaller of the two spheres. The maximum packing efficiency for random close-packing of mono-sized spheres (large or small) is approximately 64 vol%.[45–47,53,55,75–77] The corresponding interstitial void volume is therefore 36 vol%. For the case of large

* Packing efficiency is the percentage of volume occupied by the solid spheres.

spheres packed at 64 vol%, smaller spheres can be inserted into the interstitial void volume thereby increasing the packing efficiency. If the small spheres are themselves randomly close-packed in the interstitial void volume, then it too can be packed up to 64 vol%. Consequently, the maximum increase in the packing efficiency is 0.64 × 36 vol% = 23 vol%, resulting in a maximum packing efficiency of 87% for randomly close-packed bimodal-sized spheres.

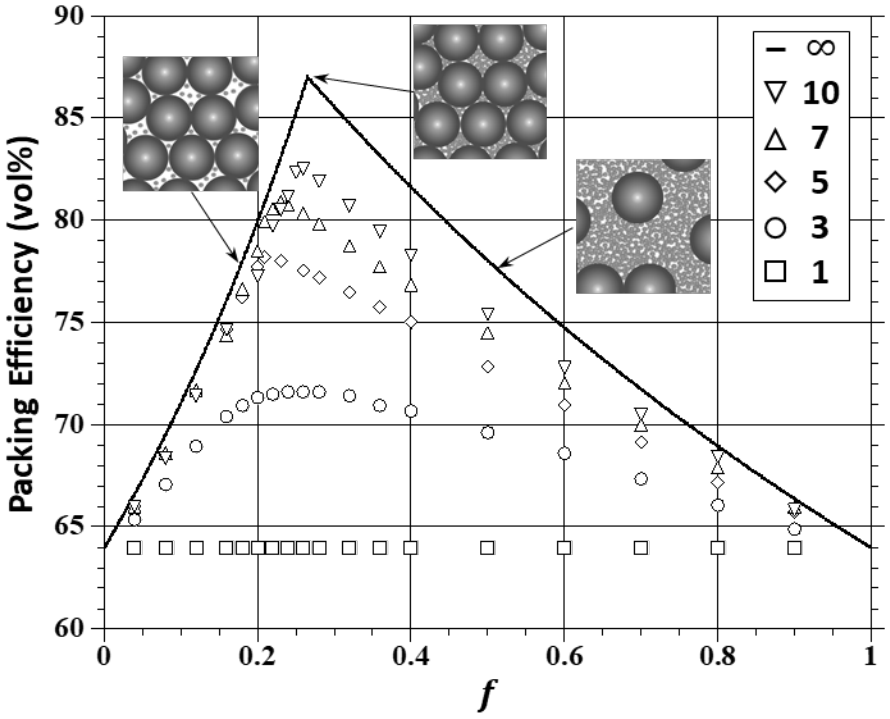

Fig. 13 Packing efficiency for bimodal-sized random close-packed spheres as a function of the fraction f of the packing efficiency made up by the smaller of the two spheres and for six large-to-small-size ratios[55]

Consider the case where large spheres are embedded in a fully dense matrix or void space at the maximum or critical volume fraction for mono-sized spheres v_{thr}^{mono}. The addition of small spheres will replace a volume of either the fully dense matrix or interstitial void space such that the total packing fraction* v_{total} can be written as

$$v_{total} = \frac{v_{thr}^{mono}}{1-f} \tag{16}$$

For randomly close-packed bimodal-sized spheres ($v_{thr}^{mono} \cong 0.64$), Eq. 16 is the solid line plotted in Fig. 13 for $0 \leq f \leq 0.265$.

* Packing fraction is the total fraction of volume occupied by the spheres.

Now consider the opposite case where the small spheres are embedded in a fully dense matrix or void space at the maximum or critical volume fraction for mono-sized spheres v_{thr}^{mono} and large spheres are being added. The addition of large spheres will replace a volume of either fully dense matrix or void space filled with small spheres at the maximum or critical volume fraction. Because the large spheres replace either fully dense matrix or interstitial void volume, the packing fraction increases. For this case, the packing fraction v_{total} can be written as

$$v_{total} = \frac{v_{thr}^{mono}}{1-(1-v_{thr}^{mono})(1-f)} \tag{17}$$

For randomly close-packed bimodal-sized spheres ($v_{thr}^{mono} \cong 0.64$), Eq. 17 is the solid line plotted in Fig. 13 for $0.265 \leq f \leq 1$.

By equating Eqs. 16 and 17, the value of $f = f_{int}$ at the intersection is given by

$$f_{int} = \frac{1-v_{thr}^{mono}}{2-v_{thr}^{mono}} \tag{18}$$

As shown in Fig. 13, for random close-packed bimodal-sized spheres, the equations intersect at $f_{int} \cong 0.265$, where the maximum packing efficiency is approximately 87%.

Though not considered in this report, plotted in Fig. 13 are estimates of the total packing fraction when size differences between the large and small spheres are finite. It is worthwhile to look at this a little further because it gives you insights into its impact on the maximum or critical inclusion volume fraction. The estimates shown in Fig. 13 are based on computational simulations of spheres filling space with sophisticated nearest-neighbor contact and stability algorithms.[55] For size differences of 5:1 (diamonds) and 10:1 (upside-down triangle), the maximum packing efficiencies are approximately 78 and 82.5 vol%, respectively, which is significantly lower than the theoretical limit of 87 vol%. Essentially, the larger the ratio of the small sphere diameter to the interstitial void space size, the less the interstitial void space can be packed efficiently with small spheres. As a result, the packing efficiency of small spheres in the interstitial void space will be vary between 0 and 64 vol% for $1 \leq {D_{large}}/{D_{small}} \leq \infty$. The case where small spheres and interstitial void space are replaced with larger spheres is more complex, because only whole spheres can be replaced, the void space contribution due to the finite curvature needs to be taken into account, and lastly, the concentration of small spheres needs to be kept constant at the critical volume fraction. In any event, the effect on the increase in packing efficiency due to the substitution of large spheres is less than the theoretical value.

The volume fraction threshold model for randomly distributed bimodal-sized inclusions is essentially given by Eqs. 16–18 with v_{thr}^{mono} approximately given by Eq. 14. This is plotted in Fig. 14 as a function of f and several $\frac{\rho_m^o}{\rho_m^{th}}$ values. The limits $f = 0$ and $f = 1$ correspond to mono-sized large and small inclusions, respectively. For $0 < f < 1$, there are both large and small inclusions. For uniaxial hot-pressing and the assumed $\frac{\rho_m^o}{\rho_m^{th}}$ values, the maximum predicted total inclusion volume fraction for bimodal-sized inclusions ranges from 0.39 to 0.51. This is significantly higher than the corresponding range for the total inclusion volume fraction for mono-sized inclusions (0.22–0.295). The predicted maxima occur at f values between 0.4 and 0.45, which is also significantly shifted from the f = 0.265 value for random close-packed bimodal spheres. The regions underneath these curves correspond to fully dense bodies, while above these curves, partially dense bodies. The last point that needs to be made here is that the predictions plotted in Fig. 14 represent the upper limits in the total inclusion volume fraction because, as discussed previously with regard to Fig. 13, finite-size-difference effects are expected to decrease this number, as well as shift where the maximum occurs.

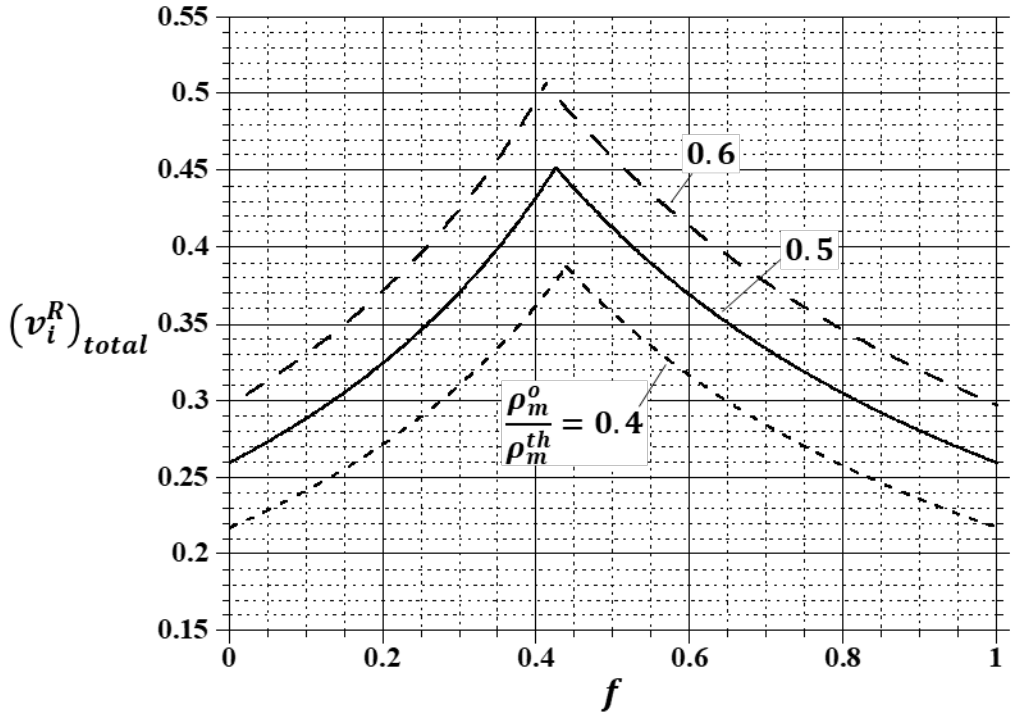

Fig. 14 Variation of the critical inclusion volume fraction with f and several $\frac{\rho_m^o}{\rho_m^{th}}$ values for randomly distributed bimodal-sized inclusions

4. Discussion and Comparison with Experiments

The motivation for this report was to address two fundamental questions concerning the hot-press densification of ceramic particulate bodies containing diamond inclusions. The first question is simply "for complete consolidation, what is the maximum diamond content that can be achieved for ceramic particulate bodies containing either mono-sized or bimodal-sized diamond inclusions?" The second important question is "on what physical parameters does this maximum diamond inclusion content depend upon?"

To address these two questions, particle-packing theory and experimental findings were initially considered. However, it was quickly realized that this only had limited application to these questions because the particles or inclusions are considered to already be in contact with one another, which is not the case. Consideration of the basic soil mechanics concept of "force chains"[74] soon led to the subject of percolation theory,[62–66] which as mentioned previously, addresses the sudden creation of extremely large clusters or highly interconnected networks in disordered systems as a result of a small change in some physical variable. As discussed earlier, the value of this physical variable at which this occurs is referred to as the percolation threshold and is accompanied by a significant change in the behavior or response of the system.

Particulate systems with randomly distributed rigid inclusions inherently possess a degree of disorder that makes percolation theory clearly applicable. For this system undergoing densification, the relevant physical variable is the volume fraction of inclusions; therefore, the percolation threshold would be the critical inclusion volume fraction where above it, the relative density is no longer 1.

The downside to percolation theory is that it is a probabilistic theory, and estimates for the percolation threshold are typically achieved numerically or computationally and therefore are not explicit functions of physical parameters. However, it was postulated that deterministic models with explicit dependencies on physical parameters could be developed by considering the uniaxial densification of the particulate composite body in terms of average characteristic physical quantities. As a result, analytical models for the conductivity and rigidity thresholds (given approximately by Eqs. 7 and 15, respectively) were developed, as well as for corresponding supercritical densification limits (Eqs. 8 and 12, respectively). The conductivity and rigidity threshold predictions are plotted together in Fig. 15 for comparison. While it should be obvious that the predictions explicitly depend on the initial relative density of the matrix $\frac{\rho_m^o}{\rho_m^{th}}$, it is implicit that they also depend on the assumed regular arrangement of inclusions, simple cubic (v_i^C) versus diamond

cubic (v_i^R). The simple cubic arrangement of inclusions was chosen because of its intuitive simplicity and the inclusion $CN = 2^*$ at the critical condition. The resulting linear chains form a continuous "conductive" path parallel to the dimension undergoing shrinkage (i.e., hot-pressing direction). Similarly, the diamond cubic was chosen because at the critical condition, the inclusions are in a tetrahedral arrangement ($CN \approx 4$), which is more structurally stable compared to the linear chain.

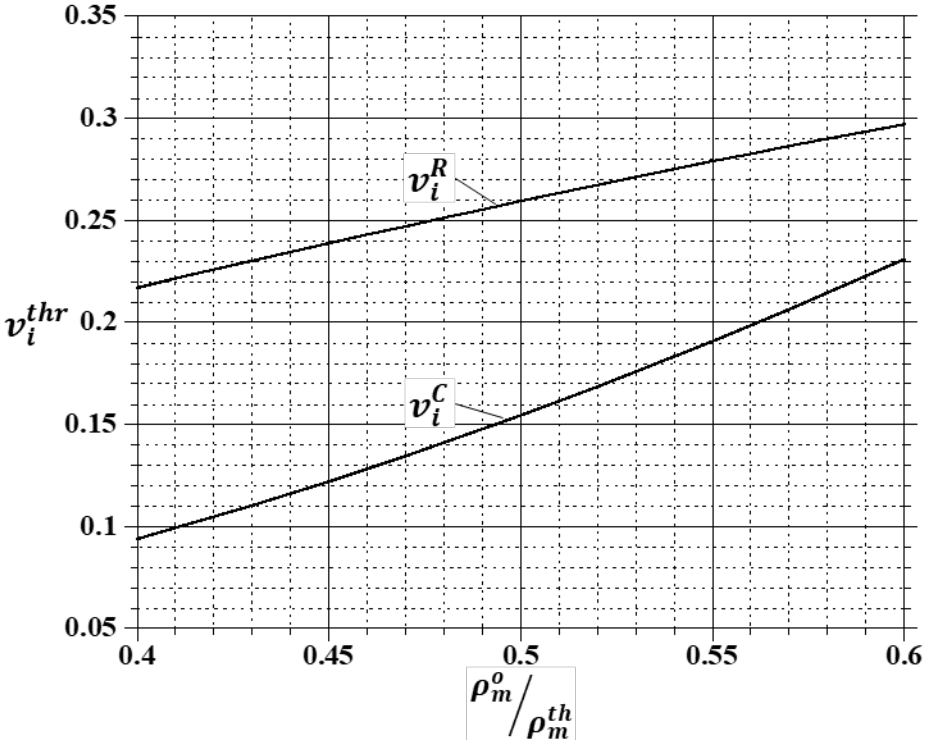

Fig. 15 Critical mono-sized inclusion volume fraction for the conductivity and rigidity threshold conditions as a function of the relative initial matrix density

4.1 Comparison of Model Threshold Predictions and Percolation Theory Predictions

So how do the predictions shown in Fig. 15 compare to percolation threshold estimates based on probabilistic models from percolation theory? In principle, it can be said that these predictions do appear to qualitatively agree with estimates from both probabilistic models[64,67,78–86] and published experimental results.[69,87–96] However, because very few models that utilize or allude to percolation theory were found in the literature, this question cannot be answered more precisely.

* Strictly speaking, the simple cubic configuration has a maximum $CN = 6$. However, at the conductivity threshold condition and uniaxial hot-pressing, the $CN = 2$.

While not completely analogous, the problem of randomly filling space with spheres has received a significant amount of attention; especially with respect to the conductivity percolation threshold.[64,67,78–82] Two primary approaches that have been used for estimating the conductivity percolation threshold for mono-sized spheres are the classical or (lattice) site percolation approach[64,78] and the continuum percolation approach.[79–81]

The site percolation approach involves superimposing a regular lattice structure into a volume of space and then randomly placing spheres at the lattice points of this structure until a connecting path from one face of the lattice to the opposite face forms. If a particle-based method is used, "inert" spheres are first placed at the lattice points, and then randomly replaced with conducting spheres. The corresponding threshold or critical volume fraction of conducting spheres is given by the sum total of their volume divided by the total volume. Depending upon the lattice structure, estimates for the conductivity percolation threshold using this approach vary between 0.14 and 0.19.[64,67,78] For a simple cubic lattice, the values vary from 0.16 to 0.19.[64,67,78]

The continuum percolation approach is more realistic than the site percolation approach in that it involves randomly filling a volume of free space (i.e., no fixed lattice sites) with inert spheres and then randomly replaced with conducting spheres until the connected path arises.[79–81] This is a more difficult problem than the site percolation problem because the resulting topologically disordered structure requires more sophisticated contact algorithms to determine the number of contacts and avoid overlapping of spheres. Also, structural stability of the system must also be considered. As a result, it is more computationally intensive. Conductivity percolation threshold estimates using this approach vary between 0.18 and 0.29.[79–81]

Models for the rigidity percolation threshold primarily use the continuum percolation approach. Due to the nature of the contacts between the rigid inclusions, the rheological behavior of the matrix in which they are embedded, and the flow or deformation condition, rigidity percolation threshold estimates possess a larger variation in values, ranging approximately from 0.2 to 0.6.[82–86] Essentially, if significant displacement or slip is possible (on the order of an inclusion diameter), as in the case of rigid inclusions in a liquid or very soft polymer, then the inclusion CN must increase to at least the six linear degrees of freedom in order to achieve a rigid structure. The corresponding critical inclusion volume fraction would therefore be above 0.5 (note that the packing fraction of a simple cubic structure [maximum $CN = 6$] is 0.52).

As mentioned previously, the conductivity and rigidity threshold predictions are in qualitative agreement with those found in the literature. Furthermore, these values are consistent with experimental findings on the densification of powders containing hard inclusions where the percolation threshold was estimated to be in the range of 0.2–0.4.[69,87–96]

4.2 Supercritical Densification Limit Predictions

Above the threshold or critical inclusion volume fraction, only partial densification is expected as shown in Figs. 7 and 12 (corresponding to Eqs. 8 and 12, respectively). If the matrix is not fully dense when the conductivity threshold condition occurs, then the inclusions can rearrange themselves enabling further densification. In this instance, the critical inclusion volume fraction will be governed by the rigidity threshold condition. In principle, further rearrangements are possible until the average inclusion $CN = 6$, which corresponds to the random close-packed configuration.

Equations 8 and 12 are plotted together in Fig. 16 for $\frac{\rho_m^o}{\rho_m^{th}} = 0.5$. Assuming for the moment that the rigidity threshold model is correct, a question that arises is that as the volume fraction of inclusions is increased above the critical threshold value, CN will also increase, and as it does, will the densification behavior eventually follow the predictions of the conductivity threshold model since the simple cubic structure has a maximum $CN = 6$ while that for the diamond cubic structure has a maximum $CN = 4$? As can be seen in Fig. 16, the supercritical densification prediction for the conductivity threshold model does cross over the prediction for the rigidity threshold model at approximately $v_i \approx 0.415$. It is hypothesized that this should be the case because as the volume fraction of inclusions increases, they become more tightly packed in the initial porous structure (see average initial inclusion spacing in Fig. 3), thereby limiting the degree to which they can rearrange. Hence, above the crossover point, the limit relative composite density should follow Eq. 8.

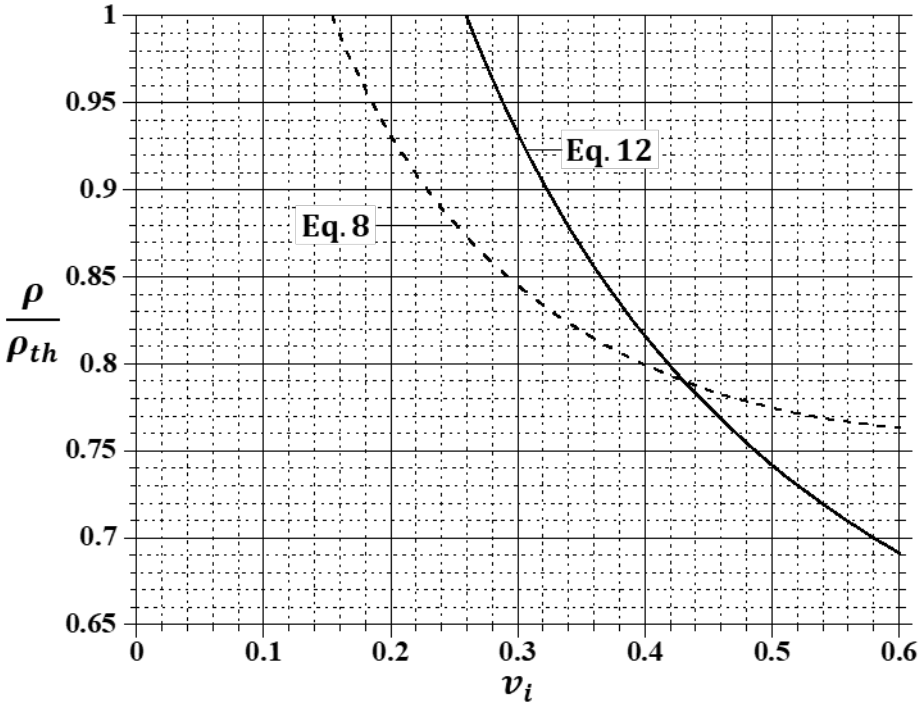

Fig. 16 Supercritical densification limit predictions for the conductivity and rigidity threshold models, Eqs. 8 and 12, respectively, with $\frac{\rho_m^o}{\rho_m^{th}} = 0.5$

4.3 Comparison of Model Predictions with Model Experiments

The models developed certainly provide answers to the questions that motivated their development. The question now considered is how well do these models predict experimental outcomes? Model predictions will be compared to experimental data; however, complete details of the experiments will not be covered here.

Hot-pressing experiments were conducted on silicon hexaboride/diamond powder mixtures at 1600 °C for 1 h under argon and an applied stress 48 MPa. Diamond inclusion sizes were 10–20 μm and 109 μm, while the silicon hexaboride particle size was less than 44 μm. For the mono-sized diamond inclusions, experiments were conducted using the 109-μm size inclusions with diamond contents of 0, 25, 30, 35, 40, 45, 50, and 55 vol%. For the bimodal-sized diamond experiments, diamond contents of 35 ($f = 0.286$), 40 (f = 0.375 and 0.4), 43.75 (f = 0.429), 45 (f = 0.4 and 0.5), and 50 (f = 0.4 and 0.5) vol% were examined. Densities after hot-pressing were measured by a technique that is based on the use of a fine free-flowing powder that easily allows measuring the density of bodies with both closed and connected porosity. For an applied stress of 48 MPa, the initial relative density of the silicon hexaboride matrix was 0.55.

The results for the mono-sized diamond experiments are shown in Fig. 17. As can be seen, experimentally, the critical volume fraction of diamond inclusions falls very close to that predicted by the rigidity threshold model (~ 28 vol%). Above the threshold, the experimental data follow the trend predicted by the rigidity supercritical densification model very closely. However, as hypothesized, the experimental data transition to follow the trend predicted by the conductivity supercritical densification model above the crossover at approximately 41 vol%. Representative microstructures for the composites with 25 and 50 vol% diamond inclusions are shown in Fig. 18a and 18b, respectively. For the 25 vol% composite, which is below the threshold, inclusion clustering can be seen, as well as regions devoid of inclusions. Qualitatively, this is consistent with the percolation threshold concept where below the threshold, inclusion clustering and cluster size are subcritical. In contrast, for the 50 vol% composite that is above the threshold, the inclusions are more uniformly spaced with no observable inclusion-free regions and a higher relative number of inclusion-inclusion contacts. Again, this is consistent with percolation theory where above the threshold, as the inclusion content increases, the critical-sized cluster continues to grow in size due to coalescence with smaller clusters eventually leading to only one cluster existing.

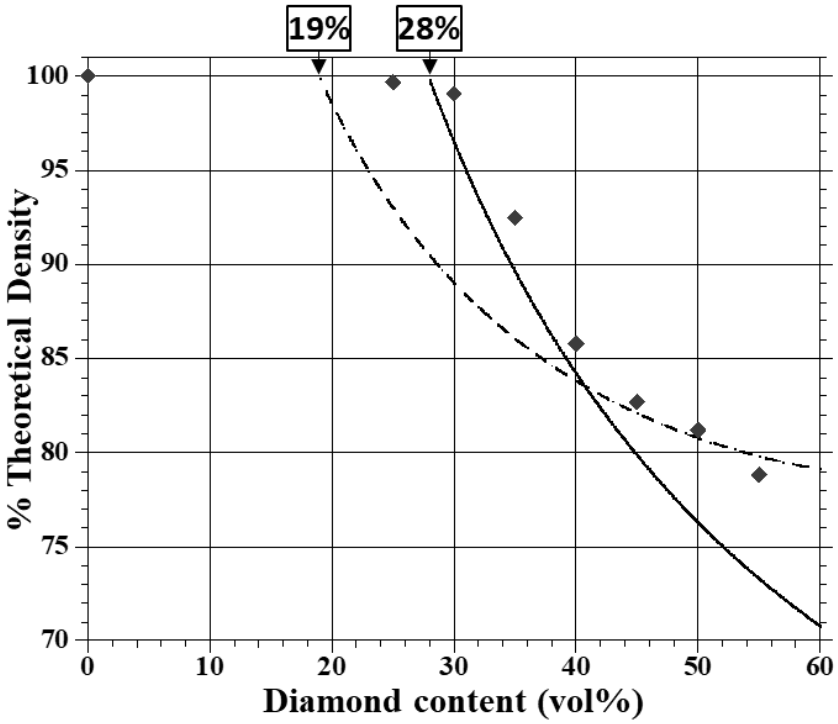

Fig. 17 Comparison of mono-sized inclusion model predictions (conductivity: dotted line; rigidity: solid line) with experimental results (diamonds) for hot-pressed mono-sized diamond inclusion–silicon hexaboride composites

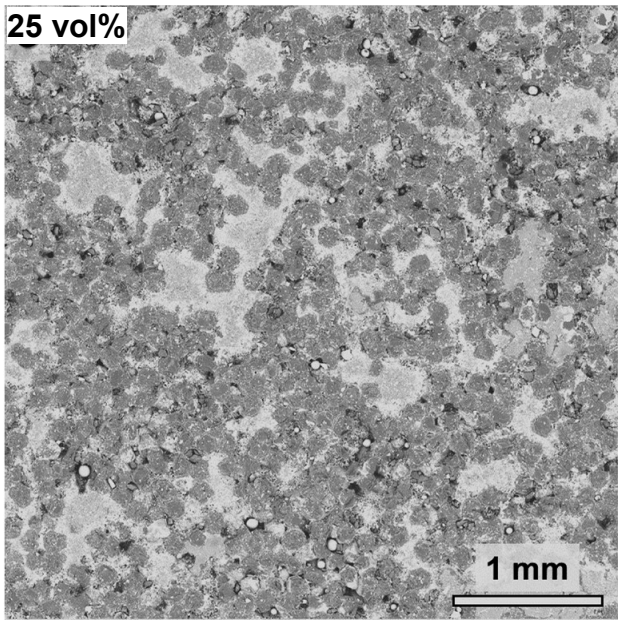

(a)

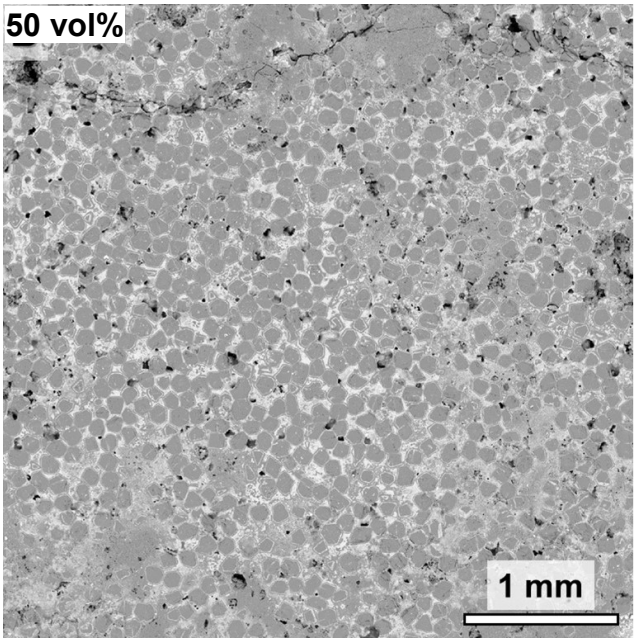

(b)

Fig. 18 Microstructures for a) 25 and b) 50 vol% diamond inclusion–silicon hexaboride composites

Turning attention to the densification results for the silicon hexaboride with bimodal-sized diamond inclusions, these are shown in Fig. 19 along with the theoretical predictions for the maximum diamond content based on the rigidity threshold model. The numbers in the boxes correspond to the measured relative densities in volume percent. For convenience, the densification data for the large

mono-sized diamond inclusions (f = 0) are also included. For the critical diamond inclusion content curve, a value for v_{thr}^{mono} = 0.28 was assumed for both the large and small diamond inclusions based on the mono-sized relative density results. Qualitatively, the experimental results are consistent with model predictions. For fixed f, relative densities decrease with increasing total diamond content, especially above the theoretically predicted threshold. For a fixed total diamond content and increasing f, relative densities increase, reaching a maximum, and then decrease. As discussed earlier in reference to Fig. 14, the predicted threshold curve is in theory expected to separate the fully dense and partially dense regions. The region beneath this curve corresponds to the fully dense region. However, as can be seen, not all of the data beneath this curve indicate a fully dense result. There are three possible explanations for this result.

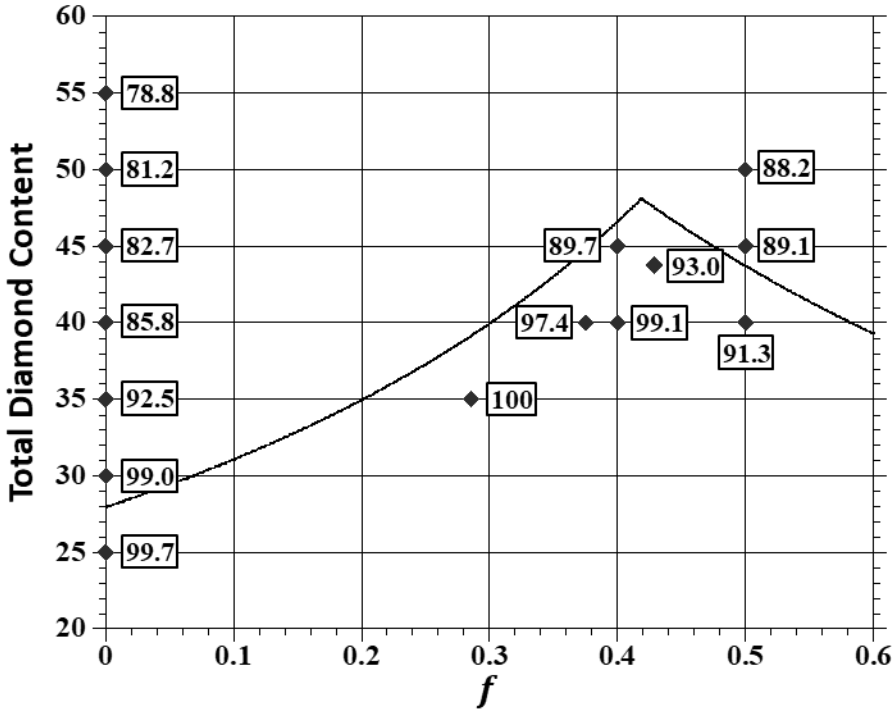

Fig. 19 Comparison of bimodal-sized rigid inclusion model predictions with experimental results for hot-pressed bimodal-sized diamond inclusion–silicon hexaboride composites

The first one to consider is based on Fig. 13 and suggests the effect of finite size differences between the large and small diamond particulates used in the hot-pressing experiments. Based on the large and small diamond particulate sizes of 109 μm and 10–20 μm, the large-to-small size ratio varies approximately between 5.5 and 11. For this range of large-to-small particulate size ratios, the maximum packing fraction also differs from the theoretical maximum by 5%–11% in Fig. 13.

If this proportionality holds true for the predicted critical diamond inclusion content curve as well, the maximum total diamond content would be expected to fall between 43 and 46 vol%.

The second explanation is that the due to the finite size difference between the small diamond particulates and the silicon hexaboride matrix particles, the threshold or critical volume fraction for the small diamond inclusions is lower than the large diamond inclusions. Essentially, because $D_{small}/d \approx 1$, it is possible for the small diamond inclusions to form a percolated network in between the silicon hexaboride particles thereby arresting densification earlier than expected. In addition, it can potentially lower the initial relative density of the matrix. This has been speculated by others as the reason for observed inclusion size effects on the densification of powders containing hard inclusions.[87,91–92,95] Its possible effect is shown in Fig. 20, where it was assumed that the threshold volume fraction for the small diamond inclusions falls within the range of 0.20–0.25 rather than 0.28. The 0.20–0.25 range for the small diamond inclusion v_{thr}^{mono} is an assumption but thought reasonable based on the large diamond inclusion relative density data shown in Figs. 17 and 18. As can be seen, the effect of a lower threshold volume fraction for the smaller diamond inclusions would shift the maximum diamond content lower and toward lower f values.

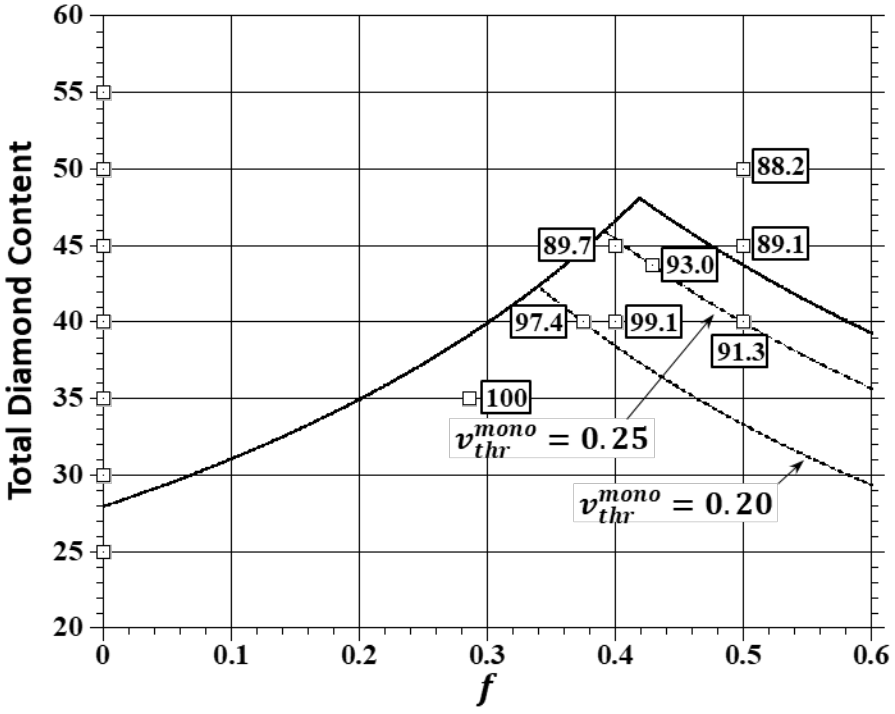

Fig. 20 Effect of a lower critical volume fraction for the small diamond inclusion due to finite-size-difference effects with respect to the silicon hexaboride particles

The last possible explanation is related to the second explanation in that as the small diamond content increases, the densification rate may be expected to decrease as a result of the decreasing the number of silicon hexaboride particle-particle contacts. This has been observed in other composite systems.[88–90,93–94,96] Hence, the effective viscosity of the composite is expected to increase significantly, thereby requiring longer times to reach full density. Close examination of the data in Fig. 19 does not strongly support this last explanation, but it should be kept in mind especially if even smaller diamond inclusion sizes are used.

While these possible explanations need to be explored in the future, the important takeaway is that the both mono-sized and bimodal-sized rigid inclusion model predictions are in very good agreement with the experimental results. Furthermore, the usefulness of the models should be self-evident, especially in guiding experiments by providing insight into the materials design space as demonstrated in Fig. 19 for bimodal-sized diamond inclusions. Imagine the case for trimodal-sized diamond particulates, which has an even larger materials design space. What should be the optimum particulate size ratios and volume fractions relative to the total diamond content? Again, models such as the ones developed and demonstrated in this report will be needed to properly address these questions and make the problem more tractable. Lastly, the differences between model predictions and experimental results stimulate the need to improve the models by taking into account issues such as finite-size differences between inclusions and matrix particles.

5. Summary and Conclusions

Simple deterministic models inspired by the conductivity and rigidity percolation threshold concepts were developed for the uniaxial densification of a composite particulate body containing either mono- or bimodal-sized rigid inclusions in order to predict the maximum inclusion content for a fully dense body. Additionally, goals included determining the physical parameters which played an important role in determining this maximum and above this maximum, what was the limit of densification.

For these models, several assumptions were made to simplify their development: 1) the particle size of the particulate matrix is much less than the rigid inclusion size; 2) the densification behavior of the particulate matrix containing randomly distributed rigid inclusions can be represented by these rigid inclusions on a regular lattice spaced by their volume averaged spacing; 3) the diamond-cubic structure with a maximum $CN = 4$ represents the rigidity threshold condition; and 4) for bimodal-sized rigid inclusions, the small inclusion size is much less than the large

inclusion size. Models for the maximum or critical inclusion volume fraction (mono- and bimodal-sized inclusions) and supercritical densification limit (mono-sized inclusions) were developed. In general, these models showed that the initial relative particulate matrix density and assumed lattice structure played an important role in determining the maximum inclusion content and the supercritical densification limit. In addition, for bimodal-sized rigid inclusions, the maximum inclusion content was strongly dependent on the fraction of this maximum made up by the smaller of the two inclusions.

When it was possible to compare model predictions to statistical-based percolation model predictions for the percolation threshold, qualitative agreements were observed. However, more importantly, excellent agreement was observed with densification data from hot-pressing experiments on mono- and bimodal-sized diamond inclusion–silicon hexaboride composite particulate bodies. Discrepancies between model predictions and experimental data for bimodal-sized rigid inclusions suggest several possible explanations centered on violations of assumptions 1) and 4) mentioned previously. These stimulate the need to develop improved models where these assumptions are relaxed.

6. References

1. Wilkins ML. Second progress report of light armor program. Livermore (CA): Lawrence Livermore Laboratory; 1967. Report No.: UCRL-50349, Rev. 1.
2. Wilkins M.L. Third progress report of light armor program. Livermore (CA): Lawrence Livermore Laboratory; 1968. Report No.: UCRL-50460.
3. Wilkins ML, Cline CF, Honodel CA. Fourth progress report of light armor program. Livermore (CA): Lawrence Livermore Laboratory; 1969. Report No.: UCRL-50694.
4. Matchen B. Applications of ceramics in armor products. Key Eng Mater. 1996;122–124:333–344.
5. Ben-Dor G, Dubinsky A, Elperin T, Frage N. Optimization of two component ceramic armor for a given impact velocity. Theo Applied Fracture Mech. 2000;33(3):185–190.
6. Lankford J Jr. The role of dynamic material properties in the performance of ceramic armor. Int J Applied Ceram Techn. 2004;1(3):205–210.
7. Hazell PJ. Ceramic armour: design and defeat mechanisms. Canberra (Australia): Argos Press; 2006.
8. Medvedovski E. Ballistic performance of armour ceramics: influence of design and structure. Part 1. Ceram Int. 2010;36(7):2103–2115.
9. Gooch Jr. WA. Overview of the development of ceramic armor technology: past, present and the future. Ceram Eng Sci Proc. 2011;32(5):195–214.
10. Krell A, Strassburger E. Order of influences on the ballistic resistance of armor ceramics and single crystals. Mater Sci Eng A. 2014;597:422–430.
11. Hazell PJ. Armour: materials, theory, and design. Boca Raton (FL): CRC Press; 2016. .
12. Shockey DA. Discussion of mechanisms of dynamic fragmentation: factors governing fragment size. Mech Mater. 1985;4(3-4):321–324.
13. Shockey DA, Marchand AH, Skaggs SR, Cort GE, Burkett MW, Parker R. Failure phenomenology of confined ceramic targets and impacting rods. Int J Impact Eng. 1990;9(3):263–275.
14. Woodward RL, Gooch WA Jr, O'Donnell RG, Perciballi WJ, Baxter BJ, Pattie SD. A study of fragmentation in the ballistic impact of ceramics. Int J Impact Eng. 1994;15(5):605–618.

15. Chen WW, Rajendran AM, Song B, Nie X. Dynamic fracture of ceramics in armor applications. J Am Ceram Soc. 2007;90(4).

16. LaSalvia JC, Campbell J, Swab JJ, McCauley JW. Beyond hardness: ceramics and ceramic-based composites for protection. J Metals. 2010;62(1):16–23.

17. Shockey DA, Simons JW, Curran DR. The damage mechanism route to better armor materials. Int J Appl Techn. 2010;7(5):566–573.

18. Appleby-Thomas GJ, Wood DC, Hameed A, Painter J, Fitzmaurice B. On the effects of powder morphology on the post-comminution ballistic strength of ceramics. Int J Impact Eng. 2017;100:46–55.

19. Flinders M, Ray D, Anderson A, Cutler RA. High-toughness silicon carbide as armor. J Am Ceram Soc. 2005;88(8):2217–2226.

20. Medvedovski E. Advanced ceramics for personnel armor: current status and future. Ceram Trans. 2006;178:1–17.

21. Mikijelj B, Chheda M, Shih J, Knoch H. Light weight ceramic armor – influence of processing on ballistic performance. Adv Sci Techn. 2006;45:1729–1738.

22. Karandikar PG. Evans G, Wong S, Aghajanian MK, Sennett M. A review of ceramics for armor applications. Ceram Eng Sci Proc. 2008;29(6):163–175.

23. Swab JJ. Recommendations for determining the hardness of armor ceramics. Int J Appl Ceram Techn. 2005;1(3):219–225.

24. Vargas-Gonzalez L, Speyer RF, Campbell J. Flexural strength, fracture toughness, and hardness of silicon carbide and boron carbide armor ceramics. Int J Appl Ceram Techn. 2010;7(5):643–651.

25. Dogan CP, Hawk JA. Role of composition and microstructure in the abrasive wear of high-alumina ceramics. Wear. 1999;(225–229):1050–1058.

26. Advanced alumina specifications brochure. Golden (CO): Coorstek; c2016. https://www.coorstek.com/media/1715/advanced-alumina-brochure.pdf.

27. Gao F. Theoretical model of intrinsic hardness. Phys Rev B. 2006;73:132104.

28. Spriggs GE. Properties of diamond and cubic boron nitride. In: Beiss P, Ruthardt R, Warlimont R, editors. Refractory, hard and intermetallic materials. Berlin Heidelberg (Germany): Springer-Verlag; 2002.

29. Swab JJ, Vargas-Gonzalez L, Wilson E, Warner E. Properties and performance of polycrystalline cubic boron nitride. Int J Appl Ceram Technol. 2015;12(S3);E74–E81.

30. MIL-STD-662F. V_{50} ballistic test for armor. Aberdeen Proving Ground (MD): Army Research Laboratory (US); 1997 Dec 18.

31. Lundberg P, Renstrom R, Lundberg B. Impact of metallic projectiles on ceramic targets: transition between interface defeat and penetration. Int J Impact Eng. 2000;24:259–275.

32. Katzman H, Libby WF. Sintered diamond compacts with a cobalt binder. Science. 1971;172:1132–1134.

33. Wentorf RH Jr, Rocco WA, inventors; General Electric Company, assignee. Diamond tools for machining. United States patent US 3,745,623. 1973.

34. Scott TA. The influence of microstructure on the mechanical properties of polycrystalline diamond: a literature review. Adv Appl Ceram. 2018;117(3):161–176.

35. National Minerals Information Center. Industrial Diamond Statistics and Information. Reston (VA): US Geological Survey; n.d. [accessed 2020 Oct 19]. https://www.usgs.gov/centers/nmic/industrial-diamond-statistics-and-information.

36. Gordeev SK, Zhukov SG, Danchukova LV, Ekstrom T, inventors; Skeleton Technologies, assignee. Method of manufacturing a diamond composite and a composite produced by same. United States patent US 6,709,747 B1. 2004.

37. Mlungwane K, Herrmann M, Sigalas I. The low-pressure infiltration of diamond by silicon to form diamond-silicon carbide composites. J Euro Ceram Soc. 2008;28:321–326.

38. Salamone S, Neill R, Aghajanian M. Si/SiC and diamond composites: microstructure-mechanical properties correlation. Ceram Eng Sci Proc. 2010;31:97–106.

39. Karandikar PG, Wong S. Microstructural design for Si-B_4C-diamond system. Ceram Eng Sci Proc. 2011;32(5):61–70.

40. Herrmann M, Matthey B, Hoehn S, Kinski I, Rafaja D, Michaelis A. Diamond-ceramics composites – new materials for a wide range of challenging applications. J Euro Ceram Soc. 2012;32(9):1915–1923.

41. Salamone S, Aghajanian M, Horner SE, Zheng JQ. Reaction bonded SiC/diamond composites: Properties and impact behavior in high strain rate applications. Ceram Eng Sci Proc. 2015;36(4):111–118.

42. Matthey B, Kunze S, Horner M, Blug B, van Geldern M, Michaelis A, Herrmann M. SiC-bonded diamond materials produced by pressureless silicon infiltration. J Mater Res. 2017;32(7):3362–3371.

43. Furnas CC. The relations between specific volume, voids, and size composition in system of broken solids of mixed size. Washington (DC): Department of Commerce, Bureau of Mines; 1928 Oct. Report of Investigations No. 2894.

44. McGeary RK. Mechanical packing of spherical particles. J Am Ceram Soc. 1961;44(10):513–522.

45. German RM. Particle packing characteristics. Princeton (NJ): Metal Powder Industries Federation; 1989.

46. Zok F, Lange FF, Porter JR. Packing density of composite powder mixtures. J Am Ceram Soc. 1991;74(8):1880–85.

47. Zheng J, Carlson WB, Reed JS. The packing density of binary powder mixtures. J Euro Ceram Soc. 1995;15:479–483.

48. Lee J-H, Lackey WJ, Benzel JF. Ternary packing of SiC and diamond particles in ethanol. J Mater Res. 1996;11(11):2804–2810.

49. Dinger DR, Funk JE. Particle-packing phenomena and their application in materials processing. MRS Bulletin. 1997;22(12):19–23.

50. Trumble KP. Spontaneous infiltration of non-cylindrical porosity: close-packed spheres. Acta Mater. 1998;46(7):2363–2367.

51. Bahraini M, Molina JM. Kida M, Weber L, Narcisco J, Mortensen A. Measuring and tailoring capillary forces during liquid metal infiltration. Current Opinion Solid State Mater Science. 2005;9:196–201.

52. Molina JM, Pinero E, Narciso J, Garcia-Cordovilla C, Louis E. Liquid metal infiltration into ceramic particle preforms with bimodal size distributions. Current Opinion Solid State Mater Sci. 2005;9:202–210.

53. Brouwers HJH. Particle-size distribution and packing fraction of geometric random packings. Phys Rev E. 2006;74:031309.

54. Leger A, Weber L, Mortensen A. Influence of the wetting angle on capillary forces in pressure infiltration. Acta Mater. 2015;91:57–69.

55. Prasad I, Santangelo C, Grason G. Subjamming transition in binary sphere mixtures. Phys Rev E. 2017;96:052905.

56. Mlungwane K. The development of a diamond-silicon carbide composite [PhD dissertation]. [Johannesburg (South Africa)]: University of the Witswatersrand; 2007. http://hdl.handle.net/10539/6937.

57. Zhu C, Lang J, Ma N. Preparation of Si-diamond-SiC composites by in-situ reactive sintering and their thermal properties. Ceram Int. 2012;38:6131–6136.

58. Hirota K, Aoki M, Kato M, Ueda M, Nakamori Y. Fabrication of diamond/SiC composites using HIP from mixtures of diamond and Si powders. Mater Res Proc. 2019;10:190–196.

59. Ceramic components. Ceramic armor components. Golden (CO): CoorsTek; c2020 [accessed 2020 Oct 20]. https://www.coorstek.com/english/industries/aerospace-and-defense/armor-components/#.

60. Performance ceramics & refractories. Military body armor. Courbevoie (France): Saint-Gobain; n.d. [accessed 2020 Oct 20]. https://www.ceramicsrefractories.saint-gobain.com/markets/defense-military-armor

61. Life critical personal protection systems. Melksham (UK): Avon Rubber p.l.c.; n.d. [accessed 2020 Oct 20]. https://www.avon-rubber.com/

62. Shante VKS, Kirkpatrick S. An introduction to percolation theory. Adv Phys. 1971;20(85):325–357.

63. Essam JW. Percolation theory. Rep Prog Phys. 1980;43:833–912.

64. Zallen R. The physics of amorphous solids. New York (NY): John Wiley; 1983. Chapter 4, The percolation model; p. 135–204.

65. Stauffer D, Aharony A. Introduction to percolation theory. London (UK): Taylor & Francis; 1991.

66. Grimmett G. Percolation and disordered systems. Berlin, Heidelberg (Germany): Springer; 1997. p. 153–300. (Lectures on probability theory and statistics, part of the lecture notes in mathematics book series, vol. 1665).

67. Lux F. Models proposed to explain the electrical conductivity of mixtures made of conductive and insulating materials. J Mater Sci. 1993;2:285–301.

68. Clingerman ML, King JA, Schulz KH, Meyers JD. Evaluation of electrical conductivity models for conductive polymer composites. J Appl Polymer Sci. 2001;83(6):1341–1356.

69. Kuo C-H, Gupta PK. Rigidity and conductivity percolation thresholds in particulate composites. Acta Metall Mater. 1995;43(1):397–403.

70. Phillips JC. Topology of covalent non-crystalline solids I: short-range order in chalcogenide alloys. J Non-Crystalline Solids. 1979;34(2):153–181 (1979).

71. Thorpe MF. Continuous deformations in random networks. J Non-Crystalline Solids. 1983;57(23):355–370.

72. Phillips JC, Thorpe MF. Constraint theory, vector percolation and glass formation. Solid State Comm. 1985;53(8):699–702.

73. Hansen A. Disorder. In: Herrmann HJ, Roux S., editors. Statistical models for the fracture of disordered media. North Holland (Netherlands): Elsevier; 1990. p. 115–158.

74. Wambaugh JF. Simple models for granular force networks. Physica D: Nonlinear Phenomena. 2010;239(18):1818–1826 (2010).

75. Baule A, Mari R, Bo L, Portal L, Makse HA. Mean-field theory of random close packings of axisymmetric particles. Nature Comm. 2013;4:2194. doi: 10.1038/ncomms3194.

76. Ni R, Stuart MAC, Dijkstra M. Pushing the glass transition towards random close packing using self-propelled hard spheres. Nature Comm. 2013;4:2704. doi: 10.1038/ncomms3704.

77. Baranau V, Tallarek U. Random-close packing limits for monodisperse and polydisperse hard spheres. Soft Matter. 2014;10:3826–3841.

78. Powell MJ. Site percolation in randomly packed spheres. Phys Rev B. 1979;20(10):4194–4198.

79. Rintoul MD, Torquato S. Precise determination of the critical threshold and exponents in a three-dimensional continuum percolation model. J Phys A: Math Gen. 1997;30:L585–L592.

80. Consiglio R, Baker DR, Paul G, Stanley HE. Continuum percolation thresholds for mixtures of spheres of different sizes. Physica A. 2003;319:49–55.

81. Rottereau M, Gimel JC, Nicolai T, Durand D. 3d Monte Carlo simulation of site-bond continuum percolation of spheres. Eur Phys J E. 2003;11:61–64.

82. Ziff RM, Torquato S. Percolation of disordered jammed sphere packings. J Phys A: Math Theor. 2017;50:085001.

83. Onoda GY, Liniger EG. Random loose packings of uniform spheres and the dilatancy onset. Phys Rev Lett. 1990;64(22):2727–2730.

84. Ellenbroek WG, Mao X. Rigidity percolation on the square lattice. Europhysics Letters. 2011;96(5):54002.

85. Liu L. Simulation of microstructural evolution during isostatic compaction of monosized spheres. J Phys D: Appl Phys. 2003;36:1881–1889.

86. Wang G. Fiore AM, Swan JW. On the viscosity of adhesive hard sphere dispersions: Critical scaling and the role of rigid contacts. J Rheology. 2019;63:229–245.

87. Lange FF. Constrained network model for predicting densification behavior of composite powders. J Mater Res. 1987;2(1):59–65.

88. Scherera GW. Sintering with rigid inclusions. J Am Ceram Soc. 1987;70(10):719–725.

89. Rahaman MN, De Jonghe LC. Effect of rigid inclusions on the sintering of glass powder compacts. J Am Ceram Soc. 1987;70(12):C-348–C-351.

90. Rahaman MN, De Jonghe LC. Sintering of particulate composites under a uniaxial stress. J Am Ceram Soc. 1990;73(3):602–606.

91. Lange FF, Atteraas L, Zok F, Porter JR. Deformation consolidation of metal powders containing steel inclusions. Acta Metall Mater. 1991;39(2):209–219.

92. Bouvard D, Lange FF. Relation between percolation and particle coordination in binary powder mixtures. Acta Metall Mater. 1991;39(12):3083–3090.

93. Fan C-L. Rahaman MN. Factors controlling the sintering of ceramic particulate composites: I, conventional processing. J Am Ceram Soc. 1992;75(8):2066–2070.

94. Jagota A, Scherer GW. Viscosities and sintering rates of composite packings of spheres. J Am Ceram Soc. 1995;78(3):521–528.

95. Bouvard D. Densification behavior of mixtures of hard and soft powders under pressure. Powder Techn. 2000;111:231–239.

96. Olmos L, Martin CL, Bouvard D. Sintering of mixtures of powders: Experiments and modelling. Powder Techn. 2009;190:134–140.

List of Symbols, Abbreviations, and Acronyms

2-D	two-dimensional
3-D	three-dimensional
Al_2O_3	aluminum oxide
A_o	cross-sectional area of cylindrical body
a_o	initial characteristic cell size for the diamond cubic structure
a^R	characteristic cell height for the diamond cubic structure at the rigidity threshold condition
B_4C	boron carbide
C	carbon
CBN	cubic boron nitride
CN	coordination number
Co	cobalt
D	inclusion diameter
D_{large}	size of large inclusions
D_{small}	size of small inclusions
d	size of matrix particles
δ_o	initial inclusion spacing in a diamond cubic structure
f	fraction of the total relative volume of inclusions made up by small inclusions
f_{int}	value of f corresponding to the maximum for v_{total}
h	height of the cylindrical body at any instant in time
h_o	initial height of the cylindrical body
HPHT	high pressures and high temperatures
L	average inclusion spacing at any instant in time
L_o	initial average inclusion spacing
LPHT	low pressure/high temperature

N_{h_o}	average number of inclusions in the height direction of the cylindrical body
N_i	total number of inclusions
N_i^C	number of inclusions per unit cell for the conductivity threshold structure
N_i^R	number of inclusions per unit cell for a diamond cubic structure
$\widehat{N}_{V_o}$	concentration of inclusions in the initial porous body
PCD	polycrystalline diamond composite
ρ	composite body density at any instant in time
ρ_i	inclusion density
ρ_{limit}^C	maximum composite density based on the conductivity threshold condition for supercritical inclusion volume fractions
ρ_{limit}^R	maximum composite density based on the rigidity threshold condition for supercritical inclusion volume fractions
ρ_m^o	initial density of the matrix
ρ_m^{th}	theoretical density of the fully dense matrix
ρ_o	initial density of porous composite body
ρ_{th}	theoretical density for the fully dense composite body
Si	silicon
SiC	silicon carbide
V	composite body volume at any instant in time
V^C	cell volume for the conductivity threshold structure
V^R	unit cell volume for the diamond cubic structure at the rigidity threshold condition
V_i	total volume of inclusions
V_m^o	initial volume of the porous matrix
V_o	initial volume of the porous body
V_o^R	initial cell volume for a diamond cubic structure

V_{th}	theoretical volume for the fully dense composite body
$\tilde{V}_i$	volume of one inclusion
$\hat{V}_o^R$	initial volume per inclusion for a diamond cubic structure
v_i	volume fraction of inclusions relative to the fully dense composite body
v_i^c	critical inclusion volume fraction for mono-sized inclusions corresponding to the conductivity threshold condition
v_i^R	critical inclusion volume fraction for mono-sized inclusions corresponding to the rigidity threshold condition
v_i^{thr}	critical volume fraction for mono-sized inclusions
v_m^{th}	volume fraction of the fully dense matrix
v_{thr}^{mono}	critical volume fraction for mono-sized inclusions
v_{total}	total volume fraction of bimodal-sized inclusions
$(v_i^R)_{total}$	total volume fraction of bimodal-sized inclusions corresponding to the rigidity threshold criterion

1 (PDF) DEFENSE TECHNICAL INFORMATION CTR
DTIC OCA

1 (PDF) DEVCOM ARL
FCDD RLD DCI
TECH LIB

5 (PDF) DEVCOM SC
FCDD SCP
J KIREJCZYK
FCDD SCP WI
R DILALLA
A FOURNIER
C LEWIS
FCDD SCP WP
D PHELPS

1 (PDF) PEO SOLDIER
SFAE SDR SPIE
D OTTERSON

78 (PDF) DEVCOM ARL
FCDD RLR
D STEPP
FCDD RLR E
C VARANASI
FCDD RLR EM
M BAKAS
E RUNNERSTROM
FCDD RLW
A RAWLETT
S SCHOENFELD
J ZABINSKI
FCDD RLW B
C HOPPEL
R BECKER
J CAMPBELL
P GILLICH
A TONGE
L VARGAS-GONZALEZ
FCDD RWL D
B MCWILLIAMS
FCDD RLW LH
P JANNOTTI
L MAGNESS
D MALLICK
FCDD RLW M
B CHEESEMAN
E CHIN
K CHO
W ROY
FCDD RLW MA
J SANDS
E WETZEL
FCDD RLW MB
C FOUNTZOULAS
G GAZONAS
E HERNANDEZ
J LIGDA
B LOVE
D MAGAGNOSC
J PITTARI
B POWERS
J SIETINS
FCDD RLW MC
S WALCK
FCDD RLW MD
J LA SCALA
S WALSH
FCDD RLW ME
K BEHLER
V BLAIR
R BRENNAN
S COLEMAN
A DIGIOVANNI
J SYNOWCZYNSKI DUNN
M GOLT
M GUZIEWSKI
S HIRSCH
C HUBBARD
M IVILL
M KORNECKI
N KU
J LASALVIA
T PARKER
P PATEL
S RAJU
A ROSENBERGER
W SHOULDERS
S SILTON
J SWAB
FCDD RLW MF
P GOINS
C HAINES
E HORWATH
FCDD RLW MG
J LENHART
R MROZEK
E NAPADENSKY
FCDD RLW PB
J MCDONALD
S SATAPATHY
T WEERASOORIYA
FCDD RLW PC
J CAZAMIAS
D CASEM
J CLAYTON
R LEAVY
J LLOYD
T SCHARF
C WILLIAMS

FCDD RLW PD
R DONEY
K STOFFEL
FCDD RLW PE
C KRAUTHAUSER
P SWOBODA
FCDD RLW S
J CIEZAK-JENKINS
A WEST